POLITECNICO DI TORINO

Master's degree in Electronic Engineering

Master's Degree Thesis

Study of multi-mode VCSEL lasers and how their performances are affected by the external optical feedback

Supervisors

Prof. Mariangela GIOANNINI

Prof. Lorenzo COLUMBO

Ricercatrice Cristina RIMOLDI

Candidate

Lara LAGANIS

Academic Year 2023-2024

Abstract

The focus of this Master's thesis is the analysis of multi-mode VCSEL and their dynamics in the context of high data rate optical transmission. The study proposes a particular emphasis on the contribution that the external optical feedback exerts on the performances of the laser.
VCSEL is the acronym for Vertical Cavity Surface Emitting Laser, they are laser diodes that can be pumped directly by an electrical current, the emission happens in the grown direction, they have very small dimensions ($\sim$ hundreds of µm) and their cavity length is in the order of a few microns.

In the first part of the thesis, the behaviour of a single-mode and a multi-mode VCSEL are numerically simulated.
In order to do that, the evolution of some quantities for different current injected are simulated, such as the carrier density distribution and the output power.
Moreover, a time analysis has been conducted to highlight the temporal evolution of the electric field modal intensities. This analysis reveals the switching on of different modes, and after the transient phase, the attainment of a steady-state condition.
Another important feature that has been analyzed is the Relative Intensity Noise (RIN). It is a measure of the relative variation in time of an optical signal intensity, it represents the intrinsic noise of the system that can degrade the optical transmission.
For a single mode VCSEL, the RIN exhibits a characteristic peak at low frequency due to the relaxation oscillation of the system. When more than one mode starts to turn on in the laser, some spurious peaks appear in the spectra due to the spatial overlapping of transverse modes.

After the characterization of the device itself, the contribution of the optical feedback has been added to the analysis. The optical feedback originates from the light reflected back into the VCSEL cavity from the optical fiber. Within the cavity, the feedback combines with the output power, introducing a modulation that is a periodic function of the phase of the back-reflected field. The effects of

the feedback include variations in the emitted power and the threshold condition, as well as changes in the carrier density and the emitted wavelength. In some cases, this has as result a further increase of the noise and then degradation of the VCSEL transmitter performances.

All these analysis are conducted using a MATLAB code to integrate an in house model developed by the supervisor research group and consisting in a set of rate equations, which is a set of differential equations that describes the evolution of the electric field intensity and of the carrier density in time.

The purpose of the second part of the thesis is to validate the code and the model used to simulate the device. In order to do that, two different approaches have been followed. The first one concerns the qualitative reproduction of the results obtained and published in the paper: *"Effects of Optical Feedback on Static and Dynamic Characteristics of Vertical-Cavity Surface-Emitting Lasers"* by Joanne Y. Law and Govind P. Agrawal, describing a similar system.
The second one includes the comparison between the code used to simulate the VCSEL and the well known Lang-Kobayashi equations used to simulate a single transverse mode semiconductor LASER under the application of simplifying hypothesis and another MATLAB code that implements the Lang-Kobayashi equations.

In the appendix, using the simplified LK model, a mathematical model has been developed to derive steady-state (continuous-wave, CW) solutions for the VCSEL system and perform the linear stability analysis on these solutions. This approach helps to identify the stability region of the CW solutions in presence of optical feedback.

Table of Contents

List of Tables

List of Figures

Chapter 1

Introduction

VCSELs were introduced in 1990 and are used mainly for short link optical data transmission in multi-mode fiber.
They are widely used due to their unique properties, such as requiring a small driving current, which leads to low power consumption and high efficiency. They exhibit excellent digital modulation behavior for high data rates and can operate effectively at high temperatures (up to 125 °C) without the need for cooling, demonstrating very high reliability and long lifetime. Additionally, their production costs are low, and they can be tested at the wafer level during the fabrication process.

Like every semiconductor lasers, VCSELs are composed by a cylindrical inner cavity where the active region consists of an hetero-structure p-i-n junction where carriers are confined in quantum wells, and an external metallizations for the supply current. The layers stack placed around the active medium is epitaxially grown perpendicular to the direction of propagation of the photons. It is composed by an alternation sequence of low and high refractive index layers that are electrically conductive and behaves as mirrors -distributed Bragg reflectors- with an high average reflectivity. Mirrors are necessary for the system to reach the lasing action. The layer structure of a VCSEL is shown in Figure 1.1.

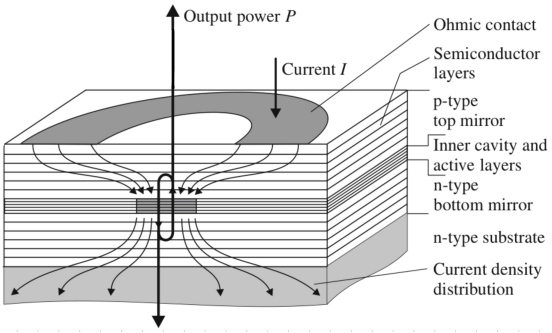

Figure 1.1: Schematic layer structure and operating principle of a VCSEL [1].

The emission wavelengths depend on the physical and geometrical characteristics of the structure. Because the VCSEL's cavity length is comparable to a single wavelength, the separation between consecutive peaks in the transmission spectrum of the inner cavity (Free Spectral Range - FSR) is very large. As a result, typically only one longitudinal mode reaches the lasing condition and is emitted.
Moreover, the transverse dimensions of the cavity determine the number of transverse mode that can propagate. Multimode lasers can afford higher power, higher robustness, and are more suitable for applications that require greater flexibility or larger beam areas. Despite the advantages of working with a multimode VCSEL, the beating between transverse higher order modes can be detrimental for error-free transmission, since it contributes to the formation of undesired peaks in the RIN spectrum [2]. The amplitude of the noise is measured through the Relative Intensity Noise spectrum.
The coherent mode coupling produces spurious peaks in the RIN spectrum, and consequently an increase in the integrated RIN measured over the receiver bandwidth. As the transmission data rate continues to rise, the bandwidth of the receivers will also need to expand. It is thus useful understanding the physical reasons behind the increase of the RIN in order to limit and to shift the spurious peaks outside the receiver's bandwidth.
It has been shown that changing the geometrical characteristics of the VCSEL allows to shift the beating's frequency outside the receiver bandwidth maintaining the advantages derived by the use of multi-mode device [3], [4], [5]. In particular, it has been shown that the elliptical oxide aperture contributes to break the quasi-degeneracy of the transverse mode associated with circular oxide aperture, shifting the spurious peaks to higher frequency. In particular, controlling the oxide aperture ellipticity and axes dimension, it is possible to modify the modal thresholds and the frequency separation among different modes [2].

This thesis aims to simulate VCSELs free running multimode behavior and evaluate

the effect of optical feedback in affecting the RIN performance. These analysis are conducted through different tests carried out with an unpublished numerical simulation code developed on MATLAB by the supervisors research group in collaboration with CISCO system.

Chapter 2

VCSEL dynamics

2.1 Model and equations

VCSELs dynamics relies on a set of differential equations describing the time evolution of the carrier's density and the electric field's amplitude and phase. The model presented in the following is taken from the paper *"Impact of Coherent Mode Coupling on Noise Performance in Elliptical Aperture VCSELs for Datacom"* written by Cristina Rimoldi, Lorenzo L. Columbo, Alberto Tibaldi, Pierluigi Debernardi, Sebastian Romero García, Christian Raabe and Mariangela Gioannini.

In all the following equations, the polar coordinate ρ is normalized to the beam waist of the fundamental mode (called C_1), $\omega_0 = \frac{2\pi c}{\lambda_0}$ is the angular frequency of the fundamental mode, and $\omega_m = 2\pi\nu_m$ is the angular frequency detuning of mode C_m with respect to the mode C_1. [2].

Equation 2.1 is the carrier's rate equation.

$$\frac{dN(\rho,\phi,t)}{dt} = \frac{\eta_i I(\rho,\phi,t)}{eV} - \frac{N(\rho,\phi,t)}{\tau_e} - \frac{n_g^2 \epsilon_0 G_N}{2\hbar\omega_0}[N(\rho,\phi,t) - N_0]\frac{|E(\rho,\phi,t)|^2}{1+\epsilon N_p(\rho,\phi,t)} + D\nabla_\perp^2 N(\rho,\phi,t) \tag{2.1}$$

The first term of the Equation 2.1 represents the carriers injection rate inside the active region, which is the region where recombining carriers contribute to photon emission. The current distribution is weighted by the injection efficiency η_i that takes into account the leakage current flowing outside the active region. V is the active region volume.
The second term represents the spontaneous emission rate, where τ_e is the carrier's lifetime.

The third term of the equations takes into account the stimulated emission, $G_N = g_N \cdot v$ where g_N is the differential gain and v the group velocity, n_g is the group refractive index, $N_p(\rho,\phi,t) = \frac{n_g^2 \epsilon_0 |E(\rho,\phi,t)|}{2\hbar\omega_0}$ is the photon density with ϵ_0 the vacuum permittivity and N_0 is the transparency carrier density.
The last term accounts for diffusion mechanism, $\nabla_\perp$ is the transverse Laplacian operator and D is the carrier diffusion coefficient.
The carrier density $N(\rho,\phi,t)$ is expanded on an orthonormal set of 91 real linear combinations of Gauss-Laguerre functions B_k [2] according to

$$N_k(t) = \int_0^\infty \int_0^{2\pi} N(\rho,\phi,t) B_k(\rho,\phi) \rho d\rho d\phi \tag{2.2}$$

Also the current distribution can be projected on the modes B_k according to

$$I_k(t) = \int_0^\infty \int_0^{2\pi} I(\rho,\phi,t) B_k(\rho,\phi) \rho d\rho d\phi \tag{2.3}$$

Substituting the carrier density components N_k and the current I_k components inside Equation 2.1 and using the orthonormality condition, it is possible to obtain the final rate equation for the modal component of the carrier density as shown in appendix A. The final rate equation is the Equation 2.4.

$$\frac{dN_k(t)}{dt} = \frac{\eta_i I_k}{eV} - \frac{N_k(t)}{\tau_e} - \frac{n_g^2 \epsilon_0 G_N}{2\hbar\omega_0} g_k(t) + d_k(t) - 4DN_k(t) q_k \tag{2.4}$$

q_k terms are defined in Appendix A.

The same procedure can be applied for the electric field rate equation (Equation 2.5), expanded on a sub set of an orthonormal basis.

$$\begin{aligned}\frac{d\tilde{E}(\rho,\phi,t)}{dt} = &-\frac{(1+i\alpha))}{2\tau_p}\tilde{E}(\rho,\phi,t) + \frac{\Gamma G_N (1+i\alpha)}{2}\frac{\tilde{E}(\rho,\phi,t)}{1+\epsilon N_p(\rho,\phi,t)}[N(\rho,\phi,t) - N_0] \\ &+ S_{sp}(\rho,\phi,t)\end{aligned} \tag{2.5}$$

The first term of Equation 2.5 is associated to mirror and waveguide losses, τ_p is the photon lifetime inside the cavity which assumes different values according to the considered transverse mode, and α is the linewidth enhancement factor (defined in Equation 2.6).

$$\alpha = -\frac{\frac{dn}{dN}}{\frac{dn_i}{dN}} = -\frac{4\pi}{\lambda}\frac{\frac{dn}{dN}}{\frac{dg}{dN}} \tag{2.6}$$

The linewidth enhancement factor describes the relative variation between the real and imaginary part of the refractive index caused by the carriers density variation.

This parameter characterizes the relative variation of the gain with respect to the refractive index.
The second term of the Equation 2.5 takes into account the stimulated emission where Γ is the longitudinal confinement factor, which represents the ratio between the power in the active region and the total power, and ϵ is the gain compression factor that takes into account the spatial hole burning phenomenon.
The last term represents the spontaneous emission contribution.

The transverse electric field profile $\tilde{E}(\rho, \phi, t)$ can be expanded on an orthonormal set of real Hermite-Gauss modes C_m that better approximate the elliptical VCSEL aperture, according to Equation 2.7.

$$\tilde{E}_m(t) = \int_0^{\infty} \int_0^{2\pi} \tilde{E}(\rho, \phi, t) C_m(\rho, \phi) \rho d\rho d\phi \tag{2.7}$$

Substituting the last expression inside Equation 2.5, and writing the the complex temporal component of the electric field in the form $E_m(t) = \tilde{E}_m(t) e^{-i\omega_m t}$, it is possible to obtain the final rate equation for the modal component of the electric field (detailed calculations are reported in Appendix A).

$$\frac{dE_m(t)}{dt} = \left(i\omega_m - \frac{1 + i\alpha}{2\tau_{p,m}} \right) E_m(t) + \frac{\Gamma G_N (1 + i\alpha)}{2} f_m(t) + S_{sp}(t) \tag{2.8}$$

Equations 2.8 and 2.4 are the set of complex coupled nonlinear differential equations for the modal component of the electric field and carriers density, with

$$f_m(t) = \int_0^{\infty} \int_0^{2\pi} \frac{E(\rho, \phi, t)}{1 + \epsilon N_p(\rho, \phi, t)} C_m(\rho, \phi) [N(\rho, \phi, t) - N_0] \rho d\rho d\phi \tag{2.9}$$

$$g_k(t) = \int_0^{\infty} \int_0^{2\pi} \frac{|E(\rho, \phi, t)|^2}{1 + \epsilon N_p(\rho, \phi, t)} B_k(\rho, \phi) [N(\rho, \phi, t) - N_0] \rho d\rho d\phi \tag{2.10}$$

$$d_k(t) = 4D \sum_n N_n(t) \int_0^{\infty} \int_0^{2\pi} B_k(\rho, \phi) B_n(\rho, \phi) \rho^3 d\rho d\phi \tag{2.11}$$

We observe that the integral term f_m (Equation 2.9) contains the physical origin for the spurious peaks in the RIN spectrum caused by the coherent overlap between different propagating transverse modes. Since the carriers density $N(\rho, \phi, t)$ has a non uniform spatial distribution and the gain compression factor ϵ is different from zero, the transverse modes interact and influence each other.

2.2 Single mode analysis

2.2.1 Parameters

The following analysis has been conducted using an in house Matlab code developed by the supervisors research group. The code has been developed to simulate multi-transverse mode dynamics, but it is possible to properly set the parameter that defines the number of propagating mode in order to obtain a single-mode simulation. This condition is forced for the current analysis, but it is physically unachievable considering the chosen pump current distribution, because the latter will generate a carrier distribution that activates multiple modes.
The simulator is based on the rate equations (Equations 2.8 and 2.4) and thus it accounts for the contribution of carrier diffusion in the transverse plane, coherent frequency mixing effects and spatial hole burning [2]. We suppose that the emitted field is linearly polarized.

The parameters used in the simulations are listed in Table 2.1, and comes from the collaboration between the research group and the CISCO Systems Inc. that has conducted experimental tests of real devices.

Parameter	Value	Parameter	Value
DBR reflectivity	0.98	Detuning ν_2	213 GHz
λ_0	850 nm	Detuning ν_3	292 GHz
N_0	$2.37 \times 10^{24}\,\mathrm{m}^{-3}$	Detuning ν_4	503 GHz
n_r (GaAs)	3.4	n_{fiber}	1.45
Active medium length	$2 \times 10^{-8}\,\mathrm{m}$	V	$7 \times 10^{-19}\,\mathrm{m}^3$
Waveguide losses α_i	$800\,\mathrm{m}^{-1}$	D	$30\,\mathrm{cm}^2\mathrm{s}^{-1}$
G_N	$7.78 \times 10^{-12}\,\mathrm{m}^3\mathrm{s}^{-1}$	$\tau_{p,1}$	1.67 ps
α	1	$\tau_{p,2}$	1.2 ps
η_i	0.76	$\tau_{p,3}$	1.13 ps
τ_e	0.92 ns	$\tau_{p,4}$	0.83 ps
Γ	0.0666	Inner cavity length	1 µm
ϵ	$1.71 \times 10^{-23}\,\mathrm{m}^3$		

Table 2.1: Parameters for dynamical simulations.

In Table 2.1, are reported the refractive index of the fiber (n_{fiber}) which represents the external cavity medium, the background refractive index (n_r), which represents the internal cavity medium, and the waveguide losses (α_i).

The supply current used to bias the VCSEL follows a supergaussian distribution, its characteristic parameters are reported in Table 2.2.

Parameters	Values
rh	4 µm
Beam waist W_0	1.79 µm

Table 2.2: Supergaussian profile parameters.

Parameter rh is defined in Equation 2.12, where r represents the radius.

$$rh = 2\rho^2 = 2\left(\frac{r}{W_0}\right)^2 \tag{2.12}$$

Equation 2.13 expresses the bias current distribution.

$$I = I_{bias} e^{-\frac{(2\rho^2)^6}{10^6}} \tag{2.13}$$

The profile shape of the bias current distribution remains consistent, while the magnitude of the flat top adjusts according to the injected current value I_{bias}. In all the reported graphs, when a current dependence is present, the indicated current value corresponds to I_{bias}.
Figure 2.1 represents the supergaussian distribution for a bias current of 8 mA.

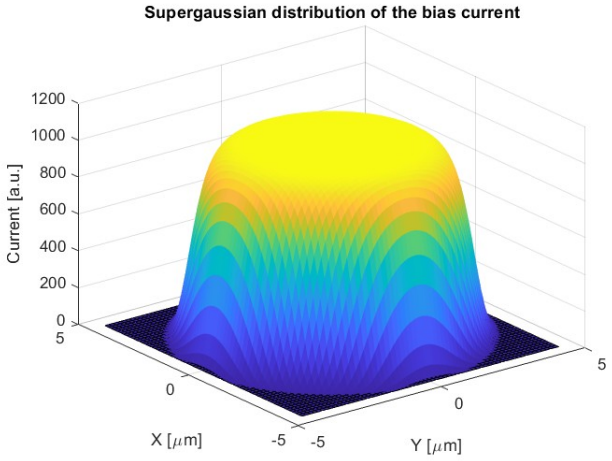

Figure 2.1: Supergaussian distribution for an injected current I=8 mA.

2.2.2 Carrier's density distribution

The quantity represented in Figure 2.2 corresponds to the difference between the overall carrier density and the transparency carrier density (namely $N - N_0$).

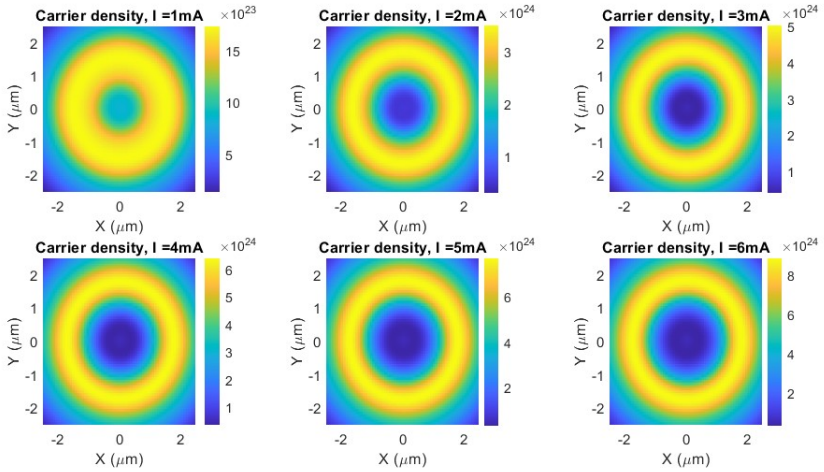

Figure 2.2: Carrier density distribution for different bias current I = [1 mA, 6 mA].

The first mode is represented in Figure 2.3 and, according to this analysis, is the only one that contributes to the emitted power.
The first mode distribution and carrier density distribution exhibit a clear correspondence: carriers recombine more in regions of higher photon density. As the injected current increases, the number of carriers within the active region rises. Also the number of carriers that recombine increases, resulting in a corresponding higher output power.

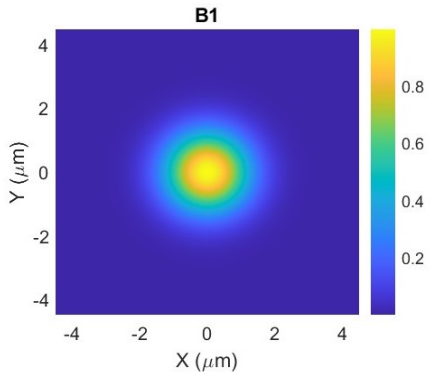

Figure 2.3: C_1 function for the first mode.

In the first analysis, zero current is injected into the device. The quantity represented in Figure 2.4 is $N - N_0$, this leads to the distribution assuming negative

values given that N is lower than the transparency carrier density. The distribution does not assume constant value (equal to N_0) because random noise is added to the normalized carrier density amplitude, independently of the input current.

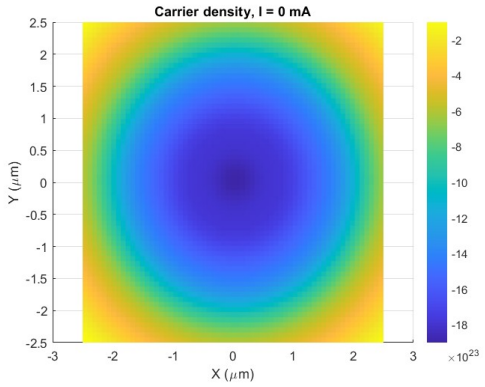

Figure 2.4: Carrier density distribution for I = 0 mA.

2.2.3 Time analysis of the modal intensities

Figures 2.5 depicts the time evolution of the modal intensity for the fundamental mode at different current values.

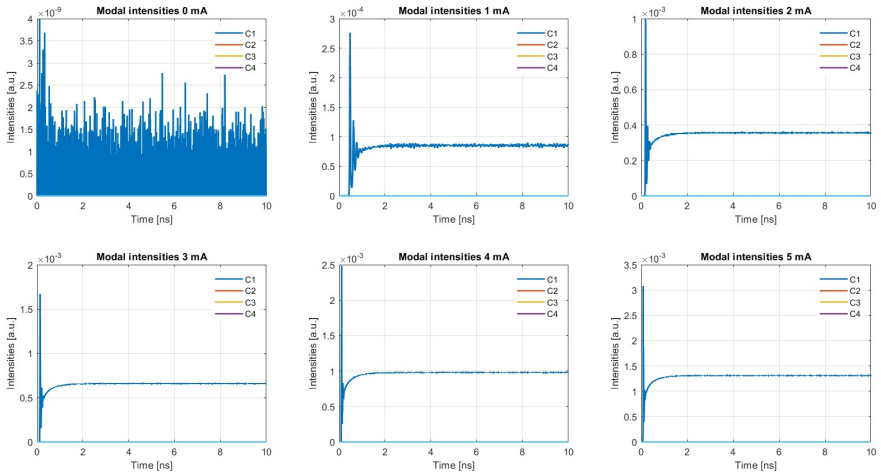

Figure 2.5: Modal intensity for an injected current going from 0 mA to 5 mA.

For zero current injected the device is below threshold, and the modal intensity consists entirely of spontaneous emission. Increasing the current and overcoming the threshold, the VCSEL switches on and starts to emit a certain amount of

optical power depending on the value of the bias current.

Figure 2.6 shows the zoom of the transient for I = 8 mA and highlights the turn-on delay of the laser. After a transient dominated by under-damped relaxation oscillations the photons reach the steady state condition.

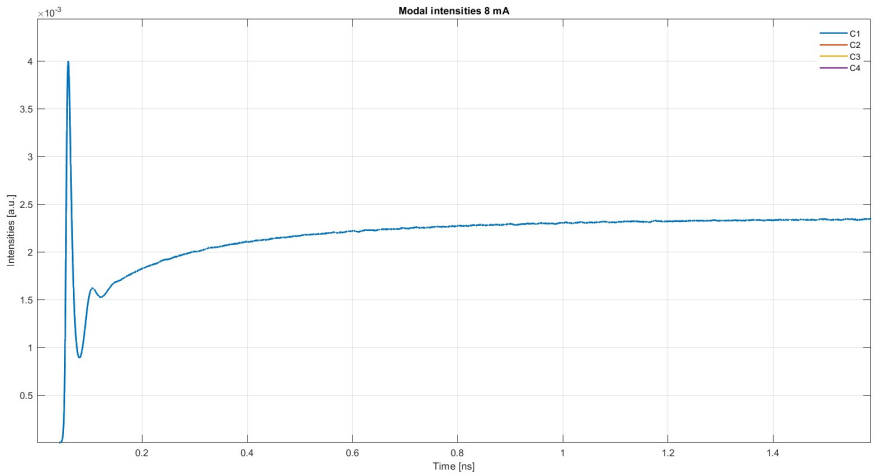

Figure 2.6: Modal intensities transient for 8 mA.

2.2.4 Output power

The output power of the device can be computed according to Equation 2.14.

$$P_{out} = \alpha_m v_g \hbar \omega V_p N_p \tag{2.14}$$

In the previous equation N_p corresponds to the photon density.
The square modulus of the normalized modal amplitudes is evaluated by summing the square of the real and imaginary parts of the normalized modal amplitude of the electric field within the specified time interval. To perform the computation, the transient period during which the electric field distribution stabilizes is excluded, and only the steady-state value is considered.
Evaluating both the real and imaginary parts of the electric field, squaring them, and summing all contributions for each propagating mode, it is possible to derive the output power characteristic as a function of the injected current.
Since the VCSEL is single mode, the normalized modal amplitude of the electric field has the same shape of the total output power represented in Figure 2.7.

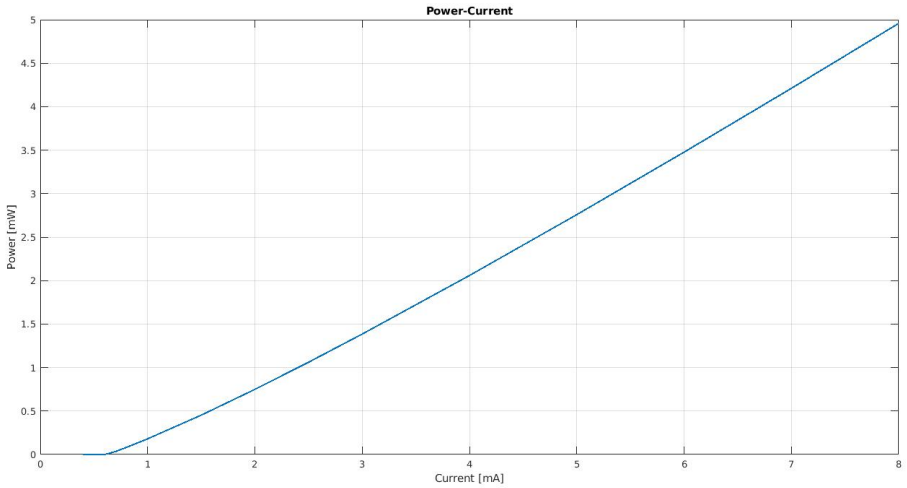

Figure 2.7: Output power.

The threshold current is around 0.7 mA. Above threshold, the power exhibits a linear dependence on the bias current as expected. The same power-current characteristic is described, for example, in the book [6].

2.2.5 RIN

Relative Intensity Noise describes the instability of power emitted by a laser. It is evaluated as the photon density fluctuations over the mean photon density squared. It depends on the injected current through the mean output power.

$$RIN_{Hz} = 10 \log_{10} \frac{2S_{\delta P(\omega)}}{P_{mean}^2} \tag{2.15}$$

Equation 2.15 describes how the RIN is evaluated, P_{mean} is the mean power over the time interval considered, $S_{\delta P(\omega)}$ represents the spectral density of the power fluctuations.
RIN spectra in Figures 2.8 are evaluated over a bandwidth of 200 GHz.

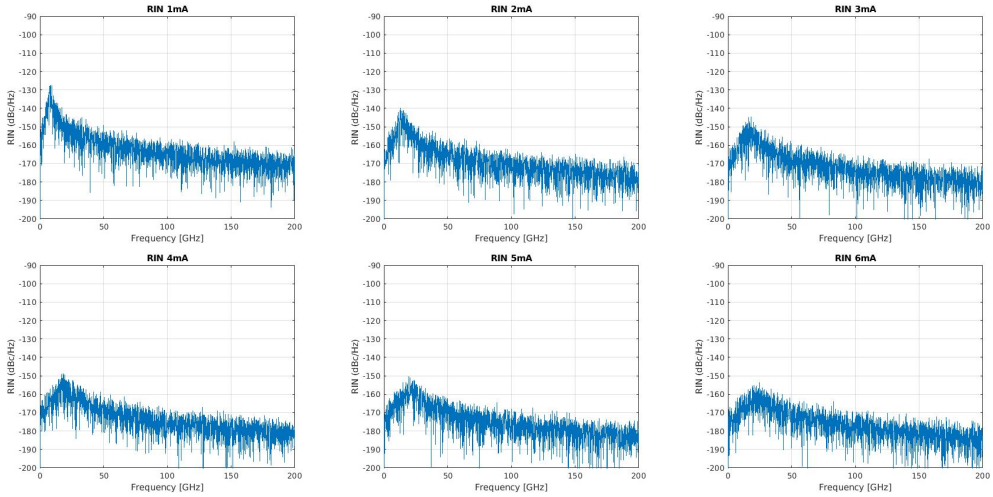

Figure 2.8: RIN for an injected current going from 1 mA to 6 mA.

As expected, the RIN spectra presents a smooth peak in correspondence to the resonance frequency due to the relaxation oscillations. The same behavior can be observed, for example, in the book [6].
The resonance frequency is around 12.5 GHz.

2.3 Multimodal analysis

In the multi-mode analysis, the parameters used are the same as those listed in Table 2.1. However, unlike in the previous section where only a single mode was involved, the first four transverse modes contribute to the transmission.
Modes considered are C_m for m = 1 - 4, and can be built through linear combinations of modes B_k [2].

$$C_1(\rho,\phi) = B_1(\rho,\phi) = \sqrt{\frac{2}{\pi}} e^{-\rho^2} \tag{2.16}$$

$$C_2(\rho,\phi) = B_2(\rho,\phi) = \sqrt{\frac{2}{\pi}} 2\rho\cos\phi e^{-\rho^2} \tag{2.17}$$

$$C_3(\rho,\phi) = B_3(\rho,\phi) = \sqrt{\frac{2}{\pi}} 2\rho\sin\phi e^{-\rho^2} \tag{2.18}$$

$$C_4(\rho,\phi) = \frac{B_4(\rho,\phi)}{\sqrt{3}} - \sqrt{\frac{2}{3}} B_5(\rho,\phi) \tag{2.19}$$

Modes that are involved in the analysis are represented in Figure 2.10.

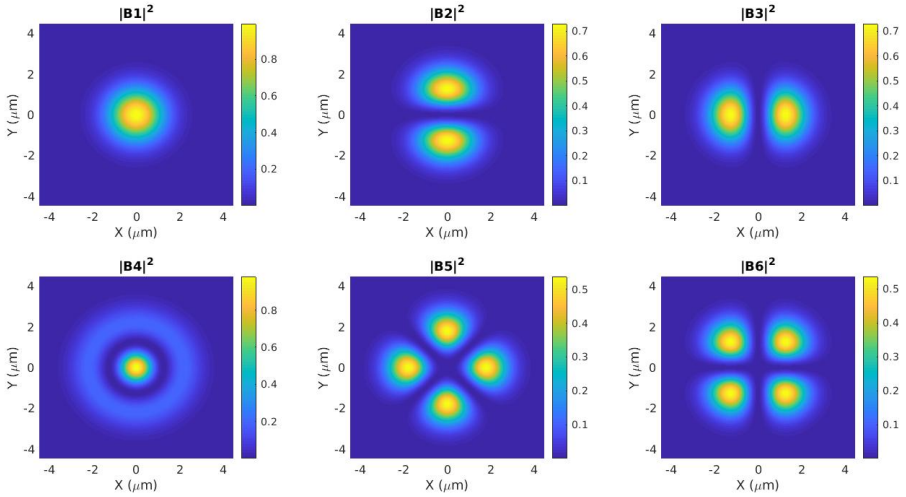

Figure 2.9: B functions.

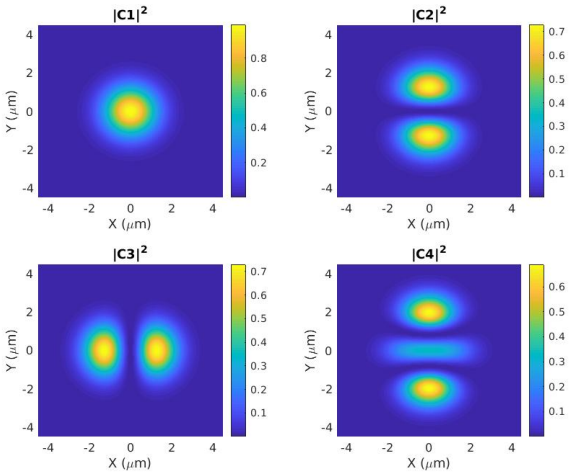

Figure 2.10: Modal distribution (C functions).

For each higher transverse mode is defined a reference frequency detuning with respect to the fundamental mode. The self-heating of the VCSEL causes a red shift of the lasing wavelengths that depends on the different transverse spatial profile. Frequency detuning values are reported in Table 2.1 and are evaluated at the threshold current for each mode [2].

2.3.1 Carrier's density distribution

Figure 2.11 shows the difference between the overall carrier density and the transparency carrier density for the multimode VCSEL.

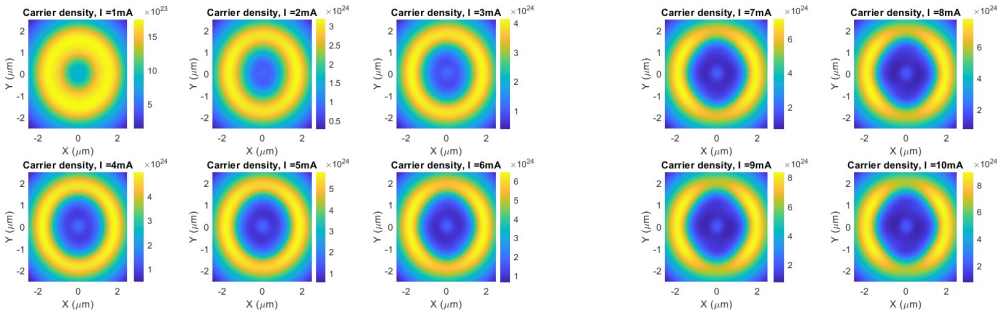

Figure 2.11: Carrier density distribution for an injected current going from 1 mA to 10 mA.

The carrier density distribution is non-uniform due to diffusion and spatial hole burning effects, which causes coupling among modes.
In order to analyze the competition between modes, the square modulus of the normalized modal amplitudes (Figure 2.12) should be analyzed. Figure 2.12 has been plotted taking into account the mean value of the modal amplitudes over the time discarding the transient for each transverse mode and considering only the steady-state condition.

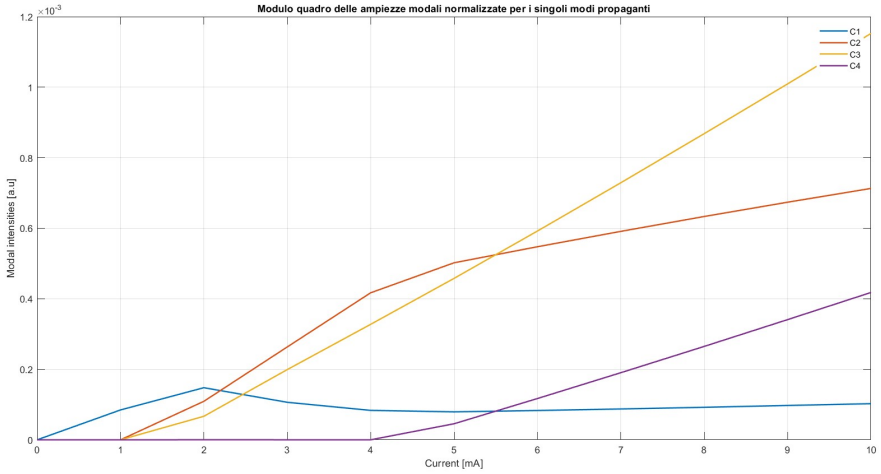

Figure 2.12: Square modulus of the normalized modal amplitudes.

From Figure 2.12 it is possible to observe that when the bias current is set to 1 mA, only the first mode contributes to the output power. For values between 2 mA and 4 mA, three lasing modes are present and only beyond 5 mA, the fourth mode becomes active.
The mode distribution and carrier density distribution exhibit a clear correspondence, with carriers recombining more in regions of higher photon density.
When the bias current is 1 mA, the fundamental mode's profile has a complementary spatial distribution with respect to the carrier's density distribution (Figure 2.9). As the second and third modes begin to be emitted, the carrier recombination increases in the central region.
From 5 mA onward, the central part, the upper and lower regions of the carrier distribution exhibit reduced carrier density following the C_4 shape. The obtained carrier's density distribution includes the contribution of all the modes.

2.3.2 Output power

Figure 2.13 shows the total optical power for the multimode configuration. Graph 2.13 has been obtained as explained in the section 2.2.4, but since four modes contribute to the output power, all of their normalized modal amplitudes should be taken into consideration for the total power evaluation.

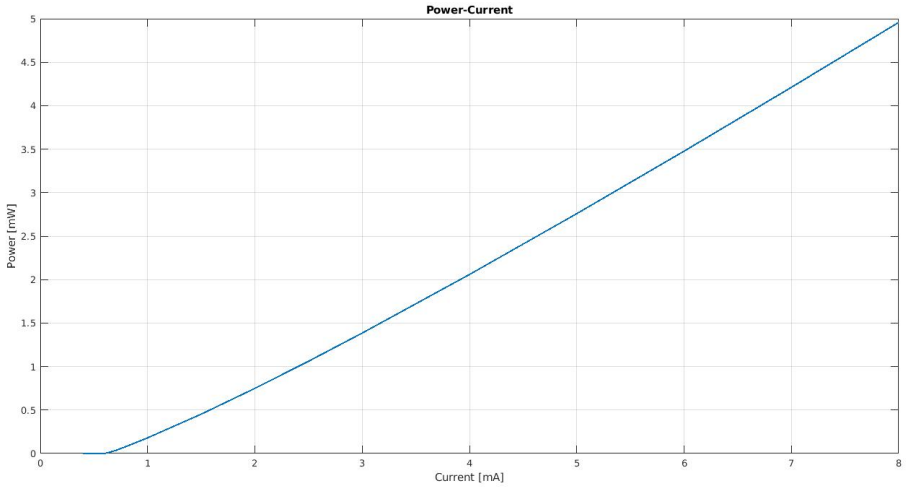

Figure 2.13: Output power.

2.3.3 Time analysis of the modal intensities

Figures 2.14 and 2.15 depict the time evolution of the modal intensity for each mode at different current values, and Figure 2.16 shows the zoom of the transient for I = 8 mA.

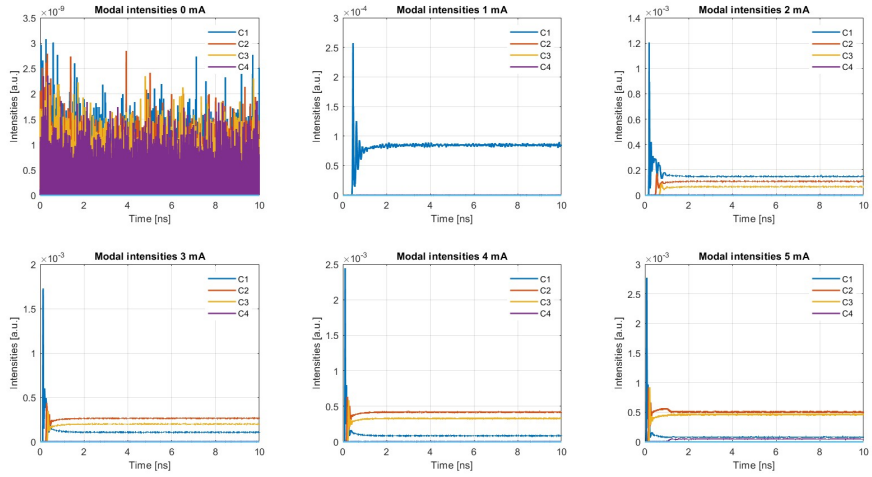

Figure 2.14: Modal intensities for an injected current going from 0 mA to 5 mA.

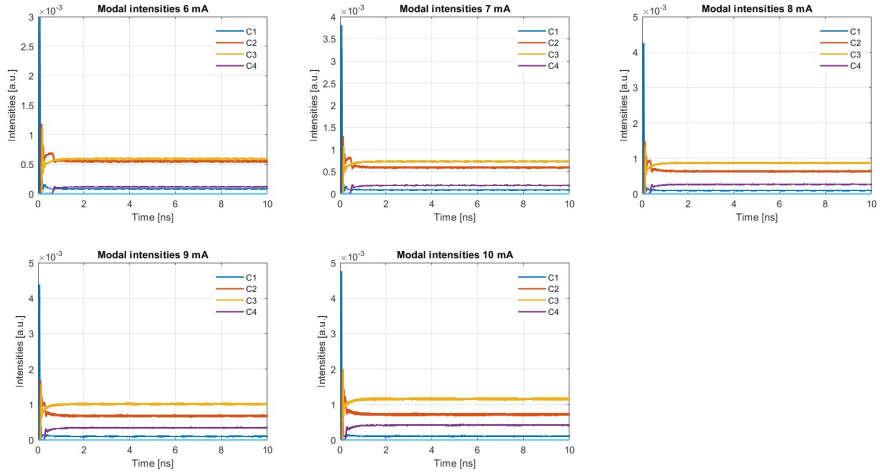

Figure 2.15: Modal intensities for an injected current going from 6 mA to 10 mA.

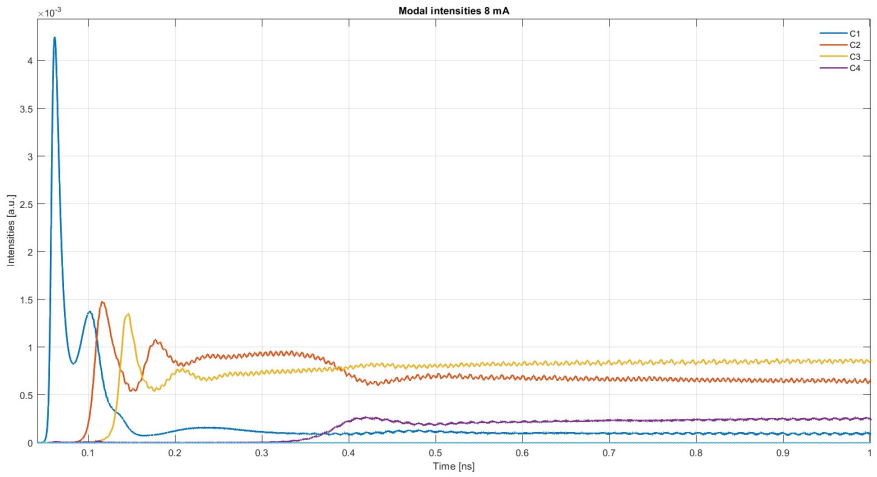

Figure 2.16: Modal intensities transient for 8 mA.

Figure 2.16 highlights the different threshold of the four modes. C_1 results partially suppressed when the second and the third mode switch on. This phenomenon can be explained by gain competition and spatial hole burning.
The gain medium in the laser has a limited amount of energy available for amplification. When the second and the third mode switch on, they compete partially for the gain resources as the first one. The fundamental mode suppression is partial because the spatial distribution of the modes do not exactly overlap, and so the spatial hole burning does not completely suppress the first mode. Moreover, as the higher order transverse modes grow, they also affect the gain distribution, leading to changes in the first mode's intensity.
If the modes overlap spatially, as happens for the C_2 and for the C_4, their interaction can reduces the effective gain for the other. The results is the reduced intensity in the temporal evolution of the already present mode.

2.3.4 RIN

Also in this case RIN is evaluated over a bandwidth of 200 GHz.

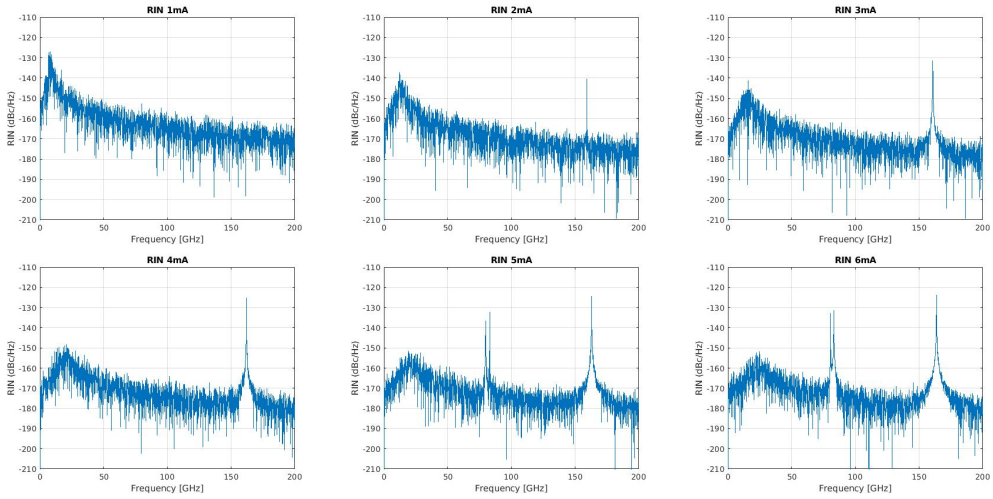

Figure 2.17: Relative intensity noise for an injected current going from 1 mA to 6 mA.

Figure 2.18 displays a superposition of two RIN spectra evaluated at low current value (4 mA) and high current value (8 mA).

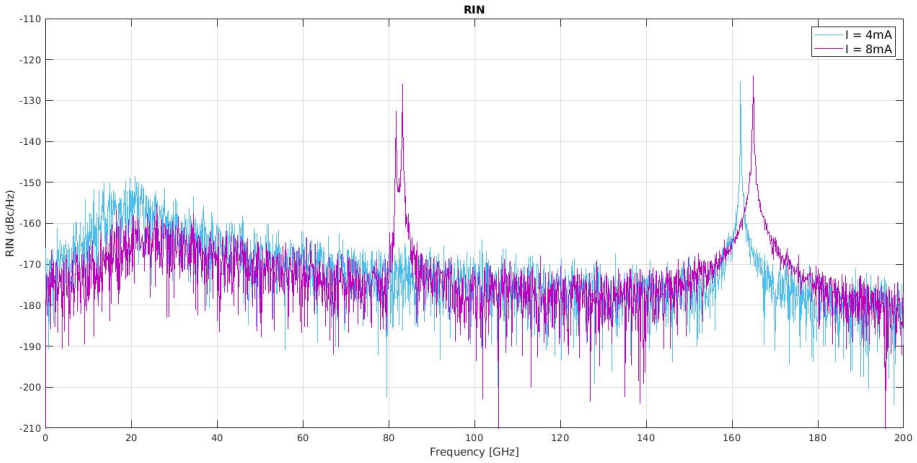

Figure 2.18: Integrated RIN for current values of 4 mA to 8 mA.

The RIN spectrum presents a smooth peak in correspondence to the resonance frequency due to the relaxation oscillations and three additional peaks due to the

spatial overlap of transverse modes. The spurious peaks appear as the current increases.
The first spurious peak emerges at 159 GHz for I = 2 mA, coinciding with the current value when the second and third modes initiate to be emitted. This peak is the results of competition between the mode C_2 and C_3. It is in fact close to the second harmonic of the frequency difference between C_3 and $C_2 = 2|\nu_3 - \nu_2|$ = 158 GHz ([2]). This peak represents the overlap between these modes and the fundamental one. Detailed calculations are reported in the paper *"Impact of Coherent Mode Coupling on Noise Performance in Elliptical Aperture VCSELs for Datacom"* written by Cristina Rimoldi, Lorenzo L. Columbo, Alberto Tibaldi, Pierluigi Debernardi, Sebastian Romero García, Christian Raabe and Mariangela Gioannini.
Meanwhile, the second and third spurious peaks arise at 80 GHz and 83 GHz, respectively, for I = 5 mA, corresponding to the onset of the fourth mode. They can be associated to the frequency difference between C_4 and $C_2 = |\nu_4 - 2\nu_2| = 80$ GHz and between C_4 and $C_3 = |\nu_4 - 2\nu_3| = 83$ GHz [2].
Peaks in RIN spectrum are associated to the non linear frequency mixing phenomenon, known as Four wave Mixing, whose efficiency depends on the spatial overlap integral between modes [2].
The overlap between modes is mediated by the non-uniform carrier distribution in the active region, as given by the term $f_m(t)$ (Equation 2.9) [2]. Spurious peaks increase the integrated RIN, whose trend of grow can be observed in Figure 2.19. Integrated RIN values for different current are also reported in Table 2.3.

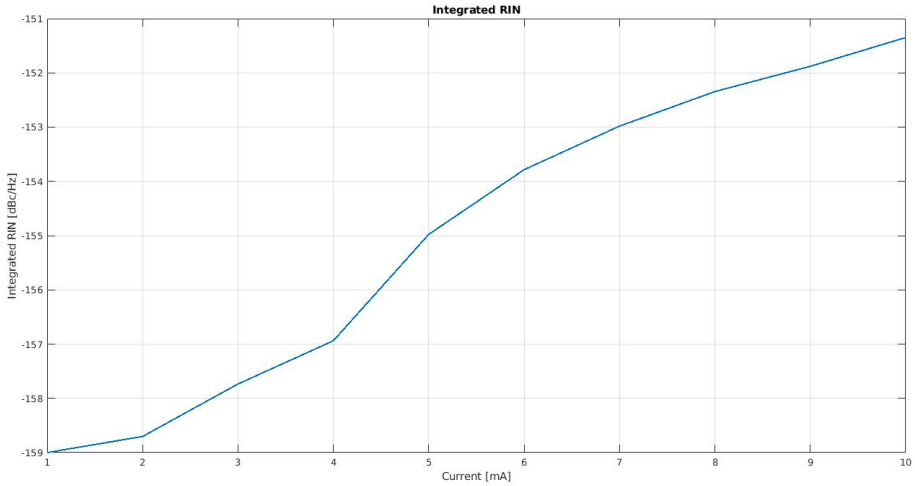

Figure 2.19: Integrated RIN for current values going from 1 mA to 10 mA.

Current [mA]	Integrated RIN [dBc/Hz]	Current [mA]	Integrated RIN [dBc/Hz]
1	-159.00	6	-153.78
2	-158.70	7	-152.98
3	-157.74	8	-152.34
4	-156.94	9	-151.88
5	-154.98	10	-151.35

Table 2.3: Integrated RIN over a bandwidth of 200 GHz.

Integrated RIN values, listed in Table 2.3, are evaluated over a bandwidth of 200 GHz. Considering a receiver bandwidth of 40-50 GHz, even for high current values (8-10 mA) the spurious peaks do not create any error in data's transmission.

Changing the detuning values listed in Table 2.1, a worse-case scenario can be achieved where the spurious peaks fall within the receiver bandwidth. Figure 2.20 shows the RIN spectrum for a current of 4.5 mA and 6 propagating modes, with the corresponding detuning values provided in Table 2.4.

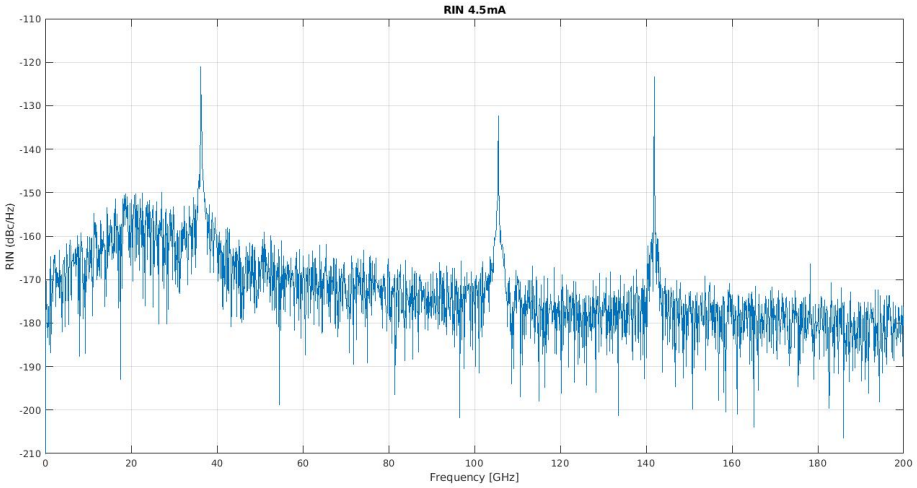

Figure 2.20: RIN spectrum.

Transverse mode	Detuning [GHz]	Transverse mode	Detuning [GHz]
C_1	0	C_4	415.528
C_2	193.521	C_5	476.125
C_3	262.111	C_6	476.125

Table 2.4: Detuning values for the 6 transverse mode.

With detuning values listed in Table 2.4 and a receiver bandwidth of 50 GHz, error during the transmission are expected due to the spurious peak that can be observed at low frequency.

Chapter 3

VCSEL dynamics with external optical feedback

The aim of this analysis is to determine how the feedback can be controlled by varying different parameters and to identify the operating regions where feedback has minimal impact on multimode VCSEL dynamics.

Physically, feedback arises from any optical elements introduced in the transmission system or from the fiber facets and junctions. Optical feedback, in a typical setup where the VCSEL is used as transmitter for optical communications, originates, for example, from the light reflected back into the VCSEL cavity from the optical fiber. Within the cavity, the feedback combines with the output power, introducing a modulation that is a periodic function of the phase of the back-reflected field.
The effects of the feedback include variations in the emitted power and the threshold condition, as well as changes in the carrier density and the emitted wavelength. Under certain conditions this may lead to an increase of noise (RIN).
Moreover, feedback introduces variation of the stationary solutions of the system, it can be another CW solution or a dynamical regime. Dynamical regime should be avoided for the transmission of information because the 1:1 correspondence between current and power is lost due to the oscillating behavior.

3.1 Model and equations

In order to extend the model described in the previous chapter for the inclusion of the external optical feedback, rate equations (Equations 2.8 and 2.4) should be modified.

The experimental setup for the feedback analysis is shown in Figure 3.1. This is similar to the experimental set-up recently proposed by Cisco system to study the effect of spurious back-reflections on the VCSEL dynamics and in particular on its RIN.

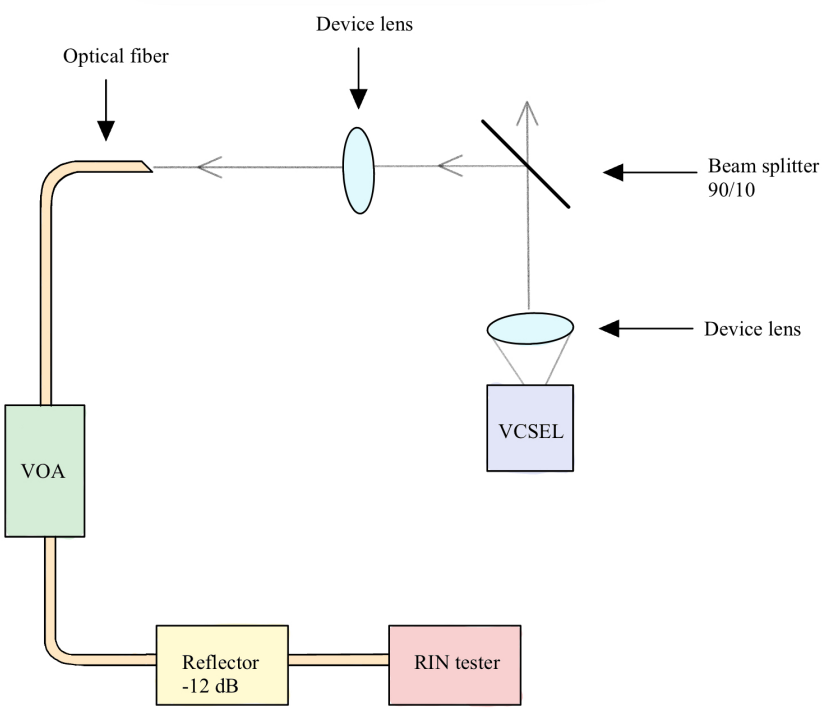

Figure 3.1: Experimental setup for feedback analysis (in collaboration with CISCO system).

The experimental setup is composed by the VCSEL, a beam splitter, a reflector and a variable optical attenuator (VOA).
The beam splitter is used to deflect the light emitted by the laser inside the optical fiber, it is included in the experimental model to prevent damage to the VCSEL when directly coupled with the fiber. Diffraction between the laser and the fiber isn't included in the model. The lenses and the beam splitter introduce experimentally a self-imaging configuration.
The reflector introduces a constant feedback inside the system, and according to experimental data, the maximum feedback value included in the analysis corresponds to -12 dB.
VOA tunes the quantity of back reflected radiation inside the system.

In the model we introduced the feedback parameter κ [7], which represents the

feedback strength.

$$\kappa_m = \epsilon\sqrt{R_{ext}}\frac{1-R}{\sqrt{R}} \tag{3.1}$$

In expression 3.1, ϵ represents the mode overlap mismatch between the back reflected and the lasing mode, it may vary depending on the mode considered, but in this model, it is assumed to be the same for all propagating modes. When ϵ is set to 1, the feedback strength reaches its maximum, with -12 dB reinjected into the system. While, when ϵ is set to 0, the configuration corresponds to that of a free-running laser.
R_{ext} is the power reflectivity of the external reflector, included in the model as $10\log_{10} R_{ext} = -12$ dB. R is the power reflectivity of the laser internal facets.
With L_{ext} we indicate the effective length that separates the VCSEL from the transmission system. In the external cavity, the modal spatial profile remains unchanged, keeping the same characteristics it has when it goes out from the VCSEL cavity. Only its modal amplitude can be modified by the feedback, this means that the approximation of negligible diffraction phenomena is applied.

The external feedback effect depends mainly on two parameters that are the κ coefficient and L_{ext}. It is possible to define the Acket'a parameter C that combines these two parameters [8].

$$C = \frac{\kappa\tau_{ext}\sqrt{1+\alpha^2}}{\tau_c} \tag{3.2}$$

Starting from field rate equations (Equation 2.8), to account for the effect of feedback, an additional time-delayed term is introduced, weighted by the coupling coefficient κ.

$$\frac{dE(t)}{dt} = (i\omega_m - \frac{1+i\alpha}{2\tau_{p,m}})E_m(t) + \frac{\Gamma G_N(1+i\alpha)}{2}f_m(t) + S_{sp}(t) + \frac{\kappa}{\tau_c}E_m(t-\tau_{ext})e^{-i\omega_0\tau_{ext}} \tag{3.3}$$

In the time delayed differential equation (Equation 3.3), τ_c and τ_{ext} are respectively the internal and external laser cavity round trip times defined in Equation 3.4 and 3.5.

$$\tau_c = \frac{2L_{cav}}{v_g} \tag{3.4}$$

$$\tau_{ext} = \frac{2n_f L_{ext}}{c} \tag{3.5}$$

The external cavity is formed by the external reflector and the VCSEL exit facet. n_f, in the Equation 3.5, is the refractive index of the external cavity medium that is close to the effective refractive index of the fiber.
Equation 3.3 includes only a single round trip through the external cavity because

the κ coefficient considered in the following analysis is small, it means that the feedback is weak and multiple reflections can be neglected. This case of weak feedback regime is the one considered during the following simulations.

The rate equation for the carrier's density is not modified by the feedback parameter, and remains the same written in Equation 2.4.

Reinjected radiation interacts with the intracavity laser field and depending on the intensity of the feedback and the phase of the reinjected field this may produce very different dynamical outputs. Figure 3.2 summarizes the five operating regimes of a laser subjected to optical feedback, boundaries between different regimes depend on the bias level and on the laser structure [8].

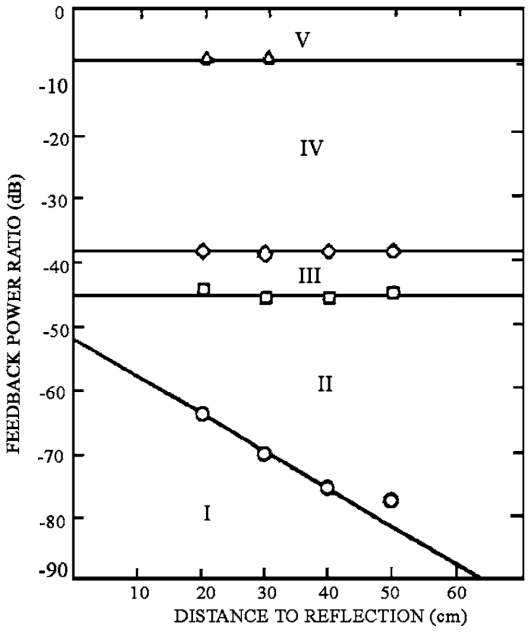

Figure 3.2: VCSEL's dynamics [8].

Regime I corresponds to the lowest feedback level, the laser operates on a single mode corresponding to the solitary laser mode narrowed or broadened depending on the phase of the feedback.
Keeping fixed L_{ext} and increasing the feedback strength, the dynamics of the VCSEL changes from single mode to multi-mode. Here the laser operates in Regime II and the modal intensity goes from being constant to oscillate regularly. The oscillation frequency of the system can be the relaxation frequency or the frequency of the external cavity $f_c = \frac{c}{2n_f L_{ext}}$. Usually the relaxation oscillations are dumped,

but due to the feedback contribution they become undamped. The rapid mode hopping between two external cavity modes is caused by noise. Since the external cavity is usually longer than the laser cavity, there is always a finite probability that the laser will jump from one available mode into another. The transition between the first and the second regime corresponds to the condition $C = 1$, this is related to multiple solutions of the steady state equation that determines the frequency of the laser [8]. The transition to the second regime is also possible keeping fixed the feedback level and increasing the length of the external cavity. For values of L_{ext} higher than a certain threshold, the laser results always unstable.
In Regime III, the laser stabilizes in a single external cavity mode with constant power output.
Increasing the feedback strength the coherence collapse region is reached. The transition to Regime IV is independent of the length of the external cavity. This Regime is characterized by a broadened optical and noise spectra and contains many external cavity modes [8].
The Regime V corresponds again to a single, stable, narrow line that is usually induced intentionally injecting inside the system high feedback levels.

The critical value of the feedback parameter κ_c defines the feedback level to inject in order to reach the instability of the laser. If the condition of long cavity regime (Equation 3.6) is verified, than κ_c can be written as Equation 3.7.

$$\omega_R \tau_{ext} >> 1 \tag{3.6}$$

$$\kappa_c = \frac{\tau_c}{2\tau_R\sqrt{1+\alpha^2}} \tag{3.7}$$

Where τ_R is defined as $\frac{1}{\Gamma_R}$, with Γ_R being the damping rate for free running laser.

$$\Gamma_R = \frac{1}{\tau_e} + \tau_p \omega_R^2 \tag{3.8}$$

Where ω_R is the angular frequency for the free running laser.

3.2 Simulation's results

In this section, the study of the dynamical regimes of a single-mode VCSEL with optical feedback is presented in terms of modal intensities temporal evolution and RIN spectra for different values of the feedback coefficient at fixed bias current I = 8 mA, that represents a typical operative bias condition.
Parameters used for the simulation are reported in Table 2.1 and correspond to parameters similar to VCSEL currently studied by CISCO system.

3.2.1 External cavity length $L_{ext} = 10cm$

In this first analysis the length of the external cavity is set at 10 cm.

Attenuation parameter $\epsilon = 1 \times 10^{-4}$

For very small values of attenuation ($\sim 10^{-4}$), the RIN spectra and the temporal evolution of the modal intensity tend to the one obtained for the free running laser analysis. The same profile can be seen in Figures 3.3 and 3.4 for the modal intensities and in Figures 3.5 and 3.6 for the RIN.

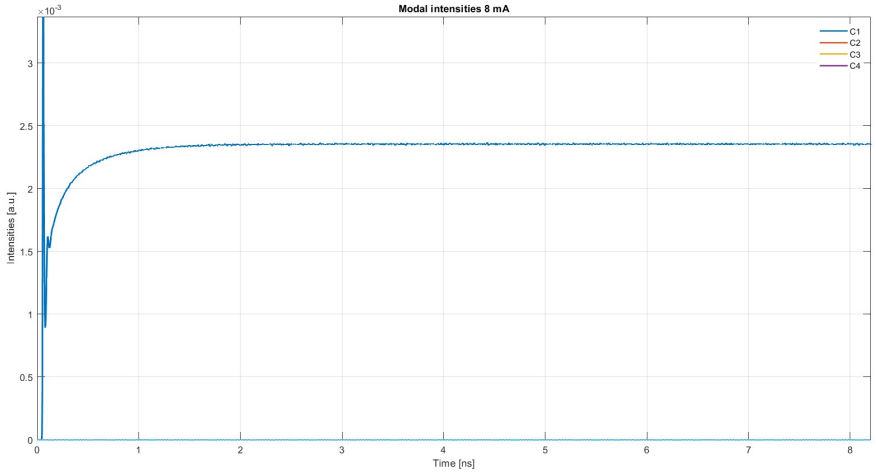

Figure 3.3: Modal intensity with $\epsilon = 0$.

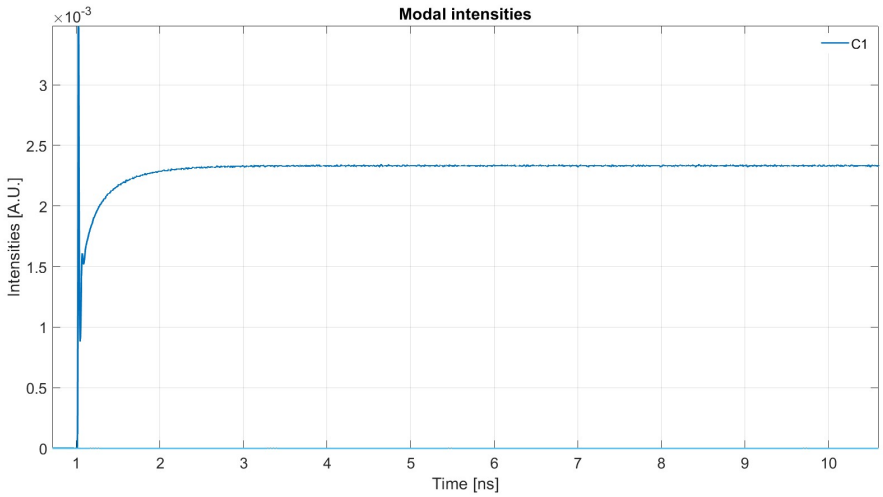

Figure 3.4: Modal intensity with $\epsilon = 10^{-4}$.

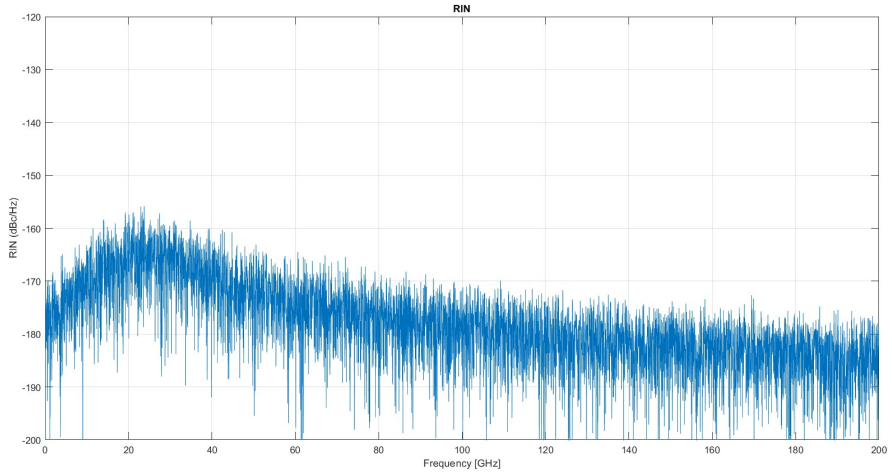

Figure 3.5: RIN with $\epsilon = 0$.

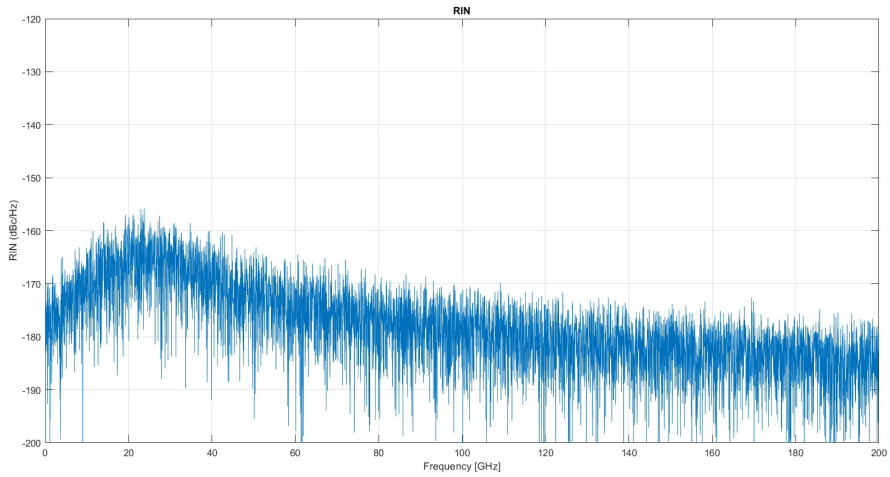

Figure 3.6: RIN with $\epsilon = 10^{-4}$.

Figure 3.5 shows the RIN spectra without feedback contribution. The smooth peak caused by the relaxation oscillation occurs around 22 GHz.

Attenuation parameter $\epsilon < 0.1$

Figures 3.7 and 3.8 show the simulation's results with $\epsilon = 0.04$ for the modal intensity and RIN spectrum. Similar evolution of the modal intensity and RIN spectrum can be observed for $\epsilon = [0.01 - 0.03]$.

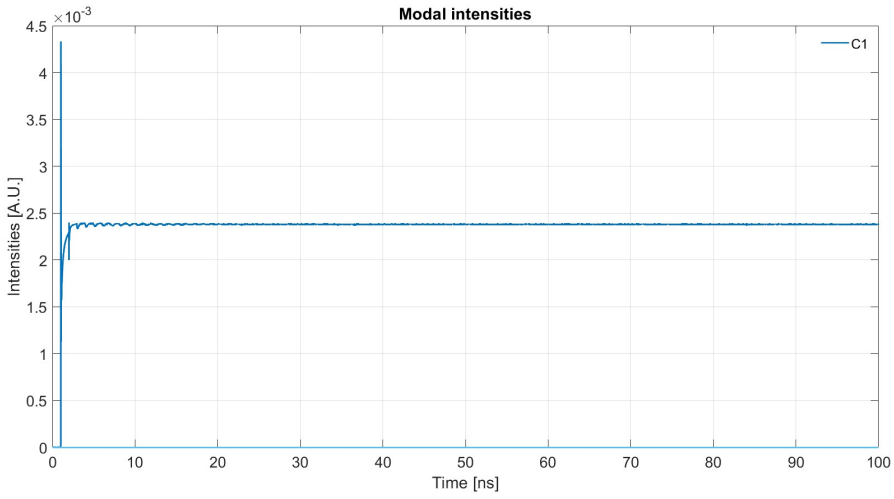

Figure 3.7: Modal intensity $\epsilon = 0.04$.

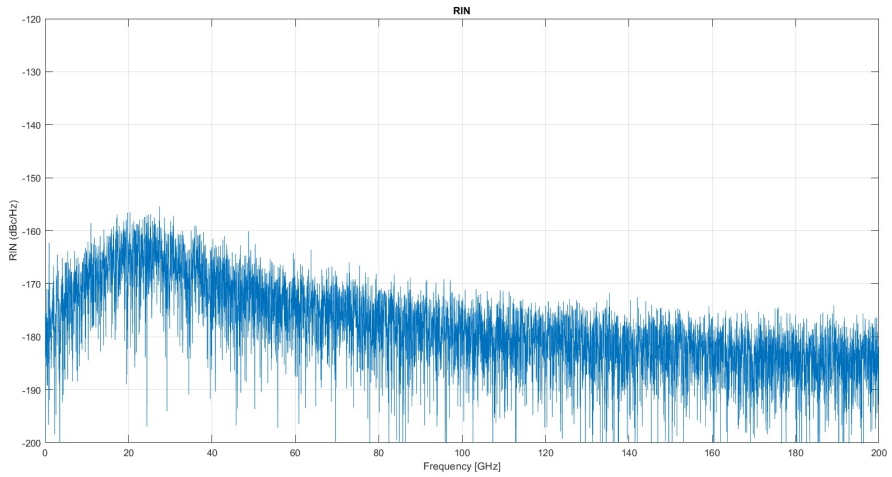

Figure 3.8: RIN spectrum $\epsilon = 0.04$.

Figures 3.9, 3.10, 3.11 and 3.12 show the simulation's results with $\epsilon = 0.05$ for the modal intensity and RIN spectrum. With $\epsilon = 0.05$ it becomes evident the presence of higher peaks in the RIN spectrum at low frequencies due to the feedback contribution.

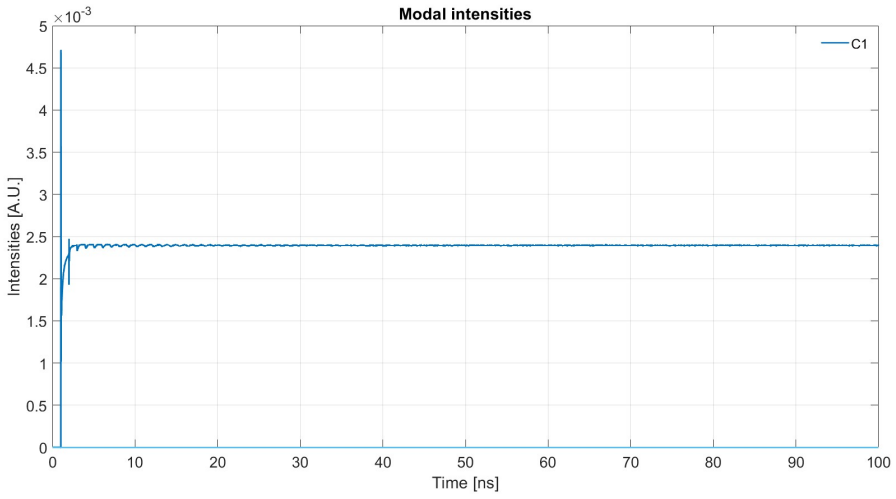

Figure 3.9: Modal intensity $\epsilon = 0.05$.

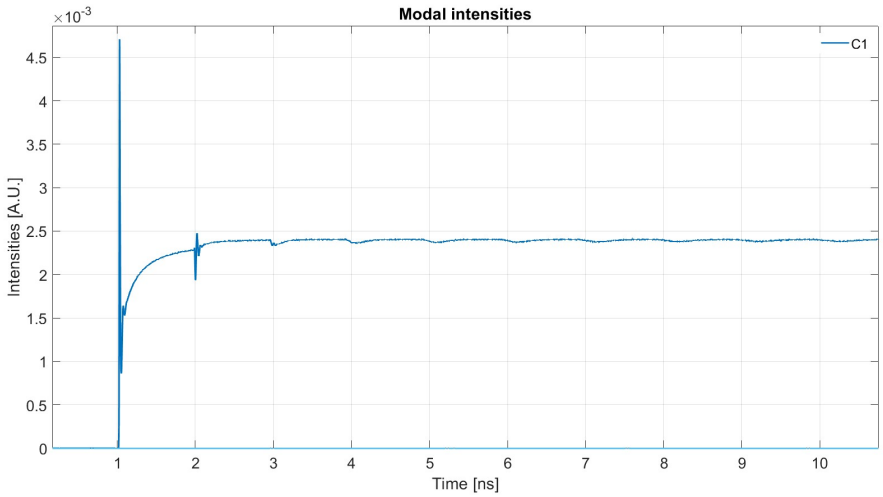

Figure 3.10: Modal intensity transient zoom $\epsilon = 0.05$.

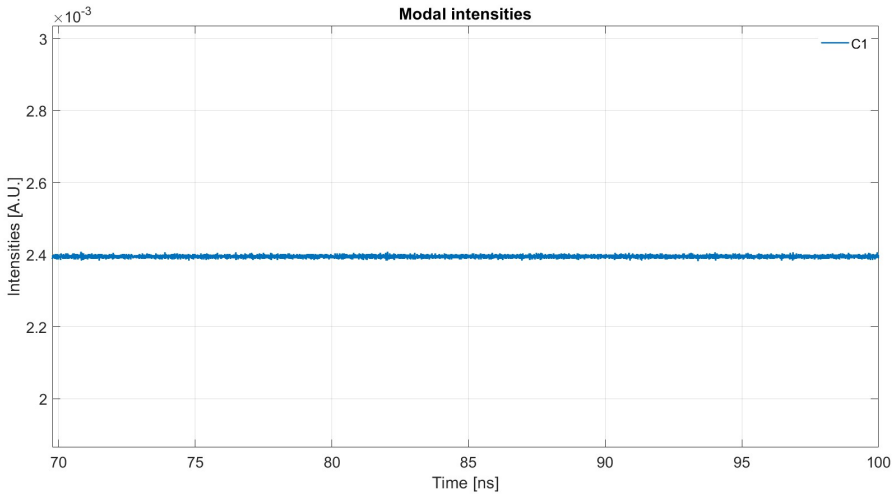

Figure 3.11: Modal intensity $\epsilon = 0.05$ zoom at 70 ns.

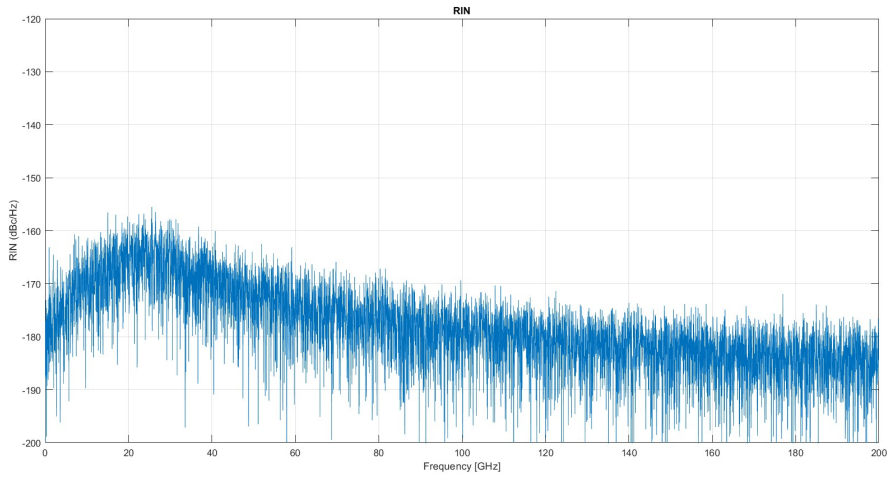

Figure 3.12: RIN spectrum $\epsilon = 0.05$.

Attenuation parameter $\epsilon = 0.1$

Figure 3.13 shows the RIN spectrum with feedback contribution with an attenuation of 0.1. At low frequencies, an increase in the RIN can be observed, along with the appearance of additional peaks, which also raises the integrated RIN.
To remove the transient from the simulation, and to be sure that the simulation has reached the steady state, the RIN spectra is evaluated for time instants above 70 ns.

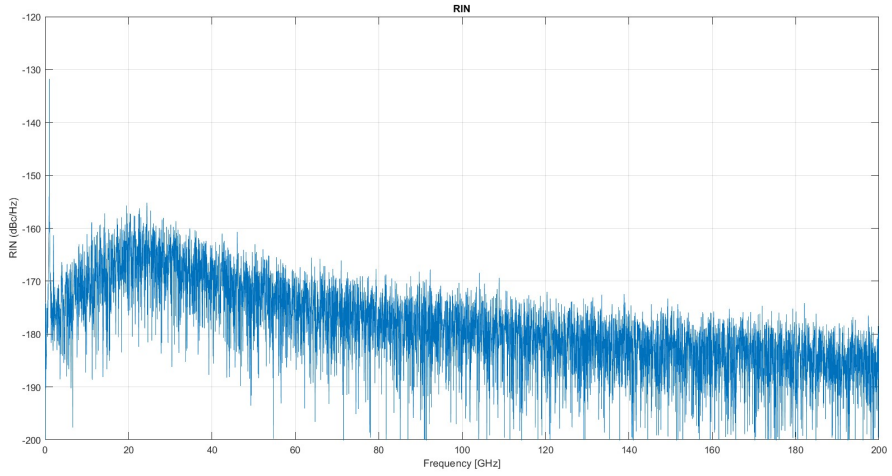

Figure 3.13: RIN spectrum with feedback ($\epsilon = 0.1$).

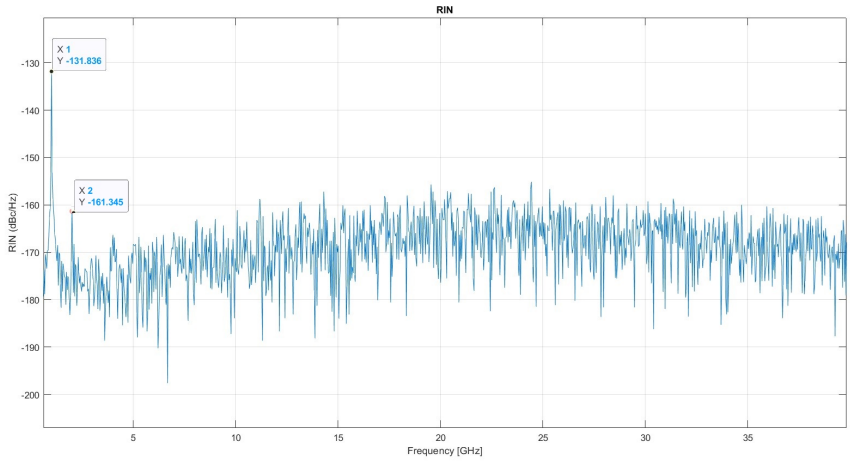

Figure 3.14: RIN spectrum with feedback ($\epsilon = 0.1$): low frequency zoom.

The external cavity frequencies correspond to values calculated using Equation 3.9.

$$FSR = \frac{c}{2n_f L_{ext}} = \frac{3 \times 10^8\,\mathrm{m/s}}{2 \cdot 1.45 \cdot 0.1\,\mathrm{m}} = 1.034\,\mathrm{GHz} \tag{3.9}$$

From Figure 3.14, it is possible to estimate that the distance between peaks at low frequency in the RIN spectra corresponds exactly to the FSR of the external cavity modes.

Figure 3.15 shows the evolution of the modal intensity of the first transverse mode with feedback contribution with an attenuation of 0.1. The spacing between the spikes within the graph corresponds to the time it takes for the field to travel twice the length of the external cavity.

$$\tau_{ext} = \frac{2n_f L_{ext}}{c} = 0.967\,\mathrm{ns} \tag{3.10}$$

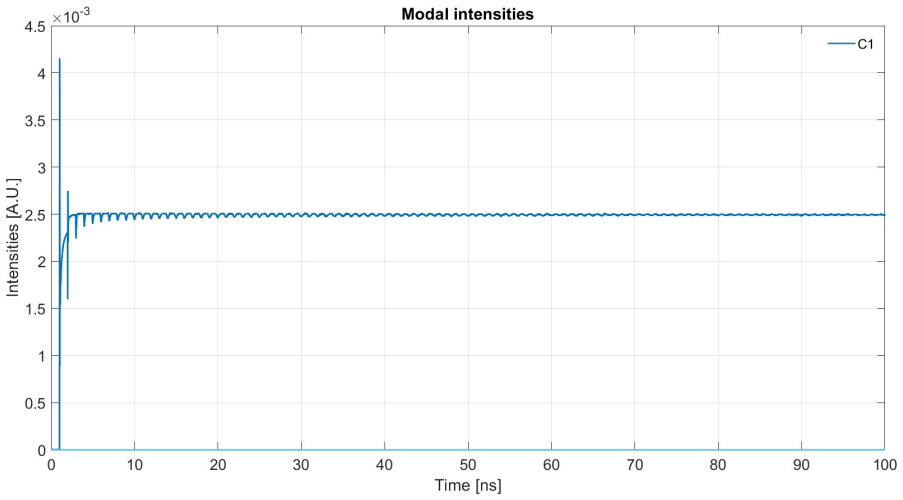

Figure 3.15: Modal intensity with feedback ($\epsilon = 0.1$).

Figure 3.16 shows a zoom in the evolution of the modal intensity of the first transverse mode with feedback contribution with an attenuation of 0.1.

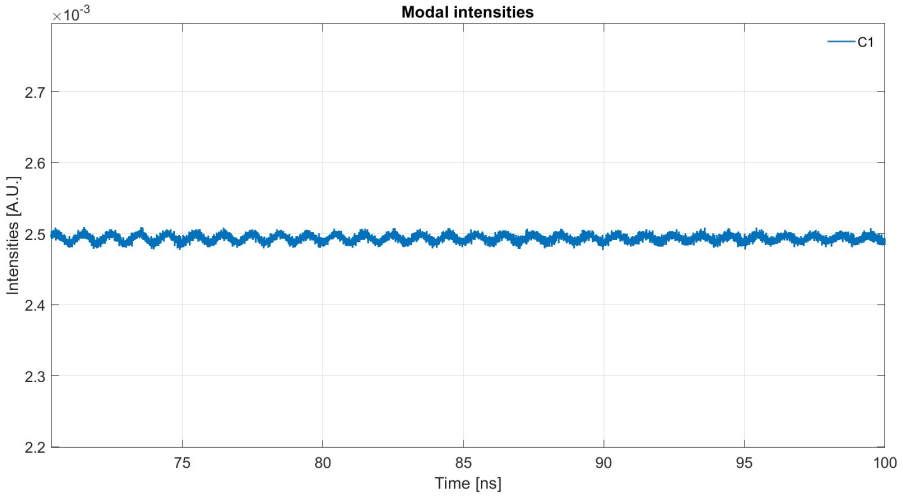

Figure 3.16: Modal intensity with feedback ($\epsilon = 0.1$): zoom at 70 ns.

Attenuation parameter $\epsilon > 0.1$

As the feedback level injected into the system increases, the transient time of the modal intensities becomes longer. Consequently, the simulation time needs to be extended to reach the steady state.

Figures 3.17, 3.18 and 3.19 show the simulation's results with $\epsilon = 0.3$ for the modal intensity and RIN spectrum.

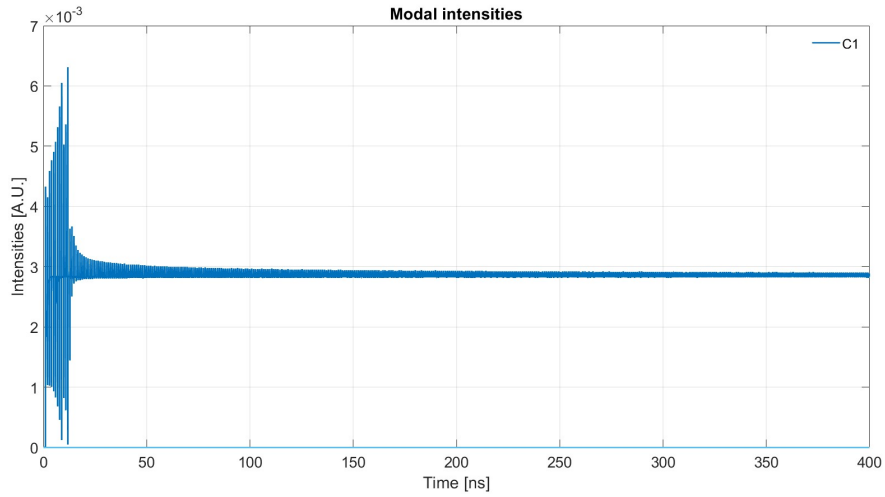

Figure 3.17: Modal intensity $\epsilon = 0.3$.

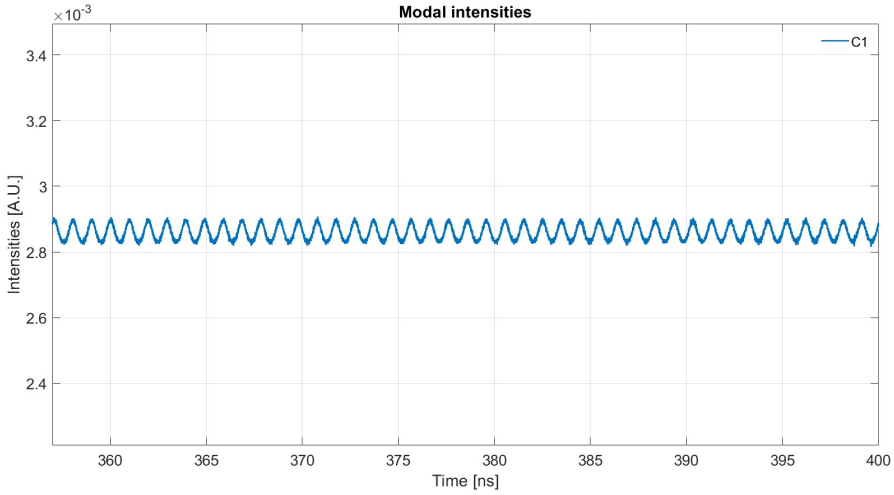

Figure 3.18: Modal intensity zoom at 370 ns, $\epsilon = 0.3$.

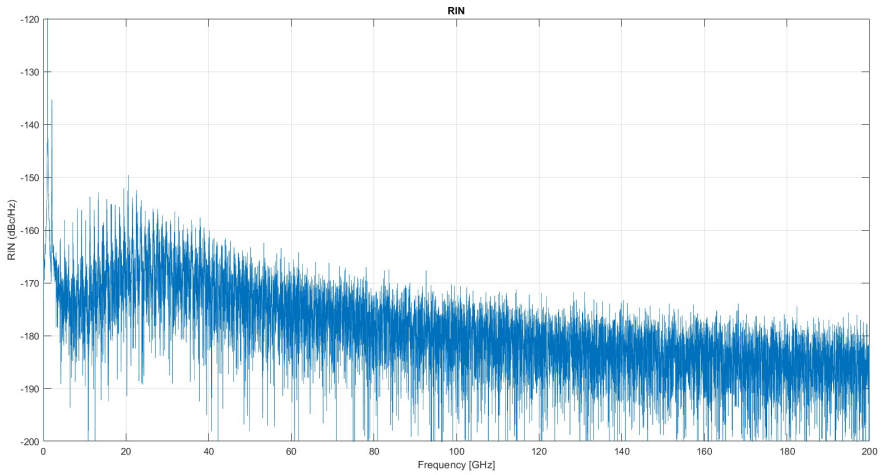

Figure 3.19: RIN spectrum $\epsilon = 0.3$.

Figures 3.20, 3.21 and 3.22 show the simulation's results with $\epsilon = 0.5$ for the modal intensity and RIN spectrum.

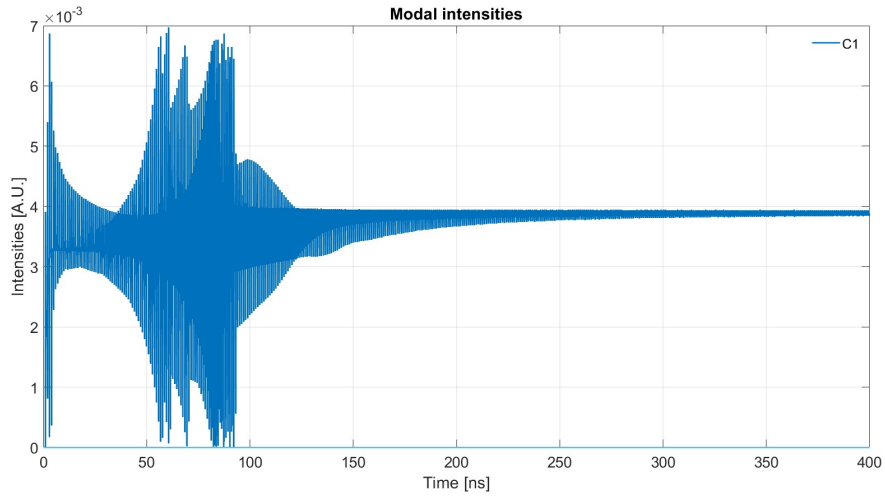

Figure 3.20: Modal intensity $\epsilon = 0.5$.

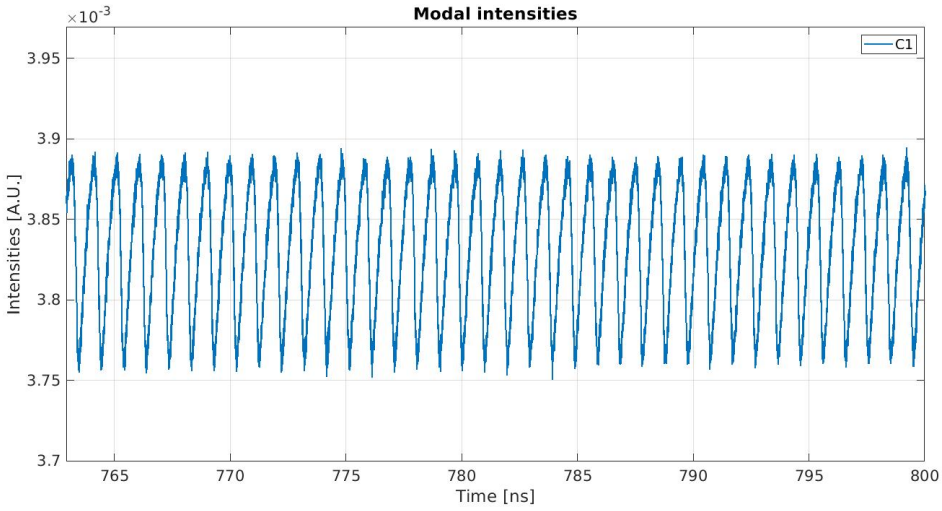

Figure 3.21: Modal intensity zoom at 770 ns ($\epsilon = 0.5$).

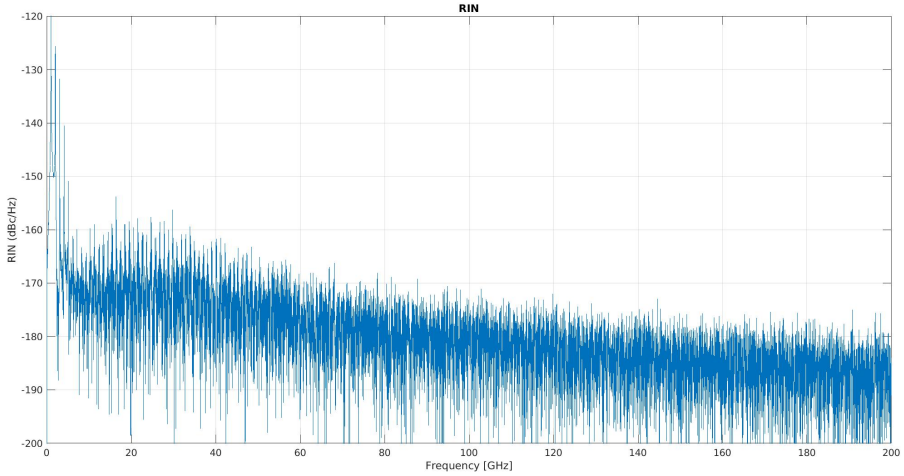

Figure 3.22: RIN spectrum $\epsilon = 0.5$.

Figures 3.23, 3.24 and 3.25 show the simulation's results with $\epsilon = 0.7$ for the modal intensity and RIN spectrum.

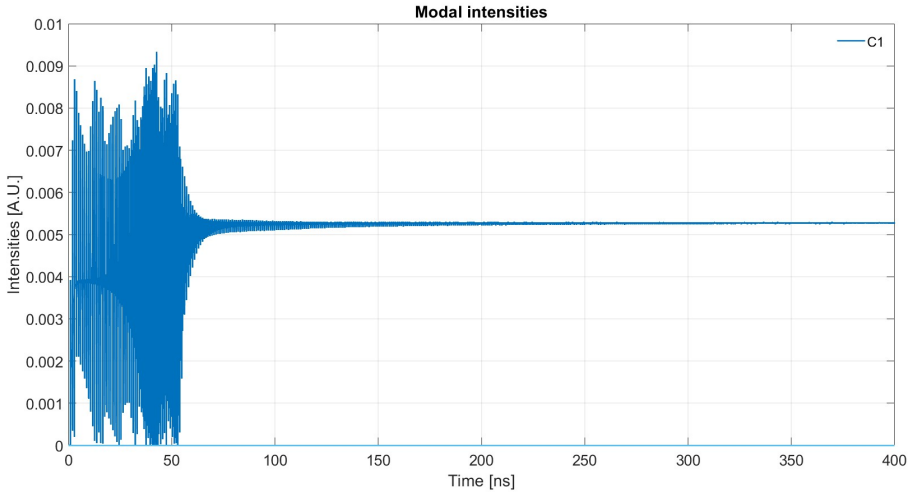

Figure 3.23: Modal intensity $\epsilon = 0.7$.

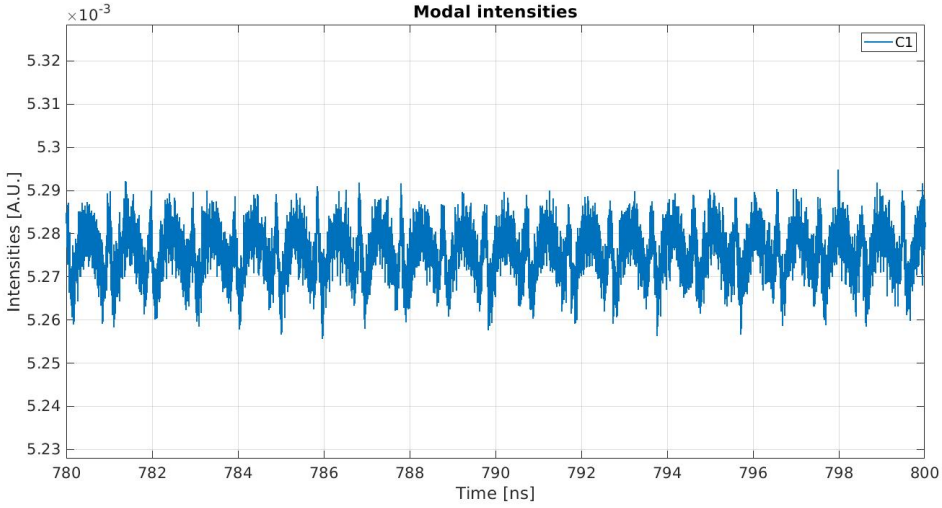

Figure 3.24: Modal intensity zoom at 770 ns, $\epsilon = 0.7$.

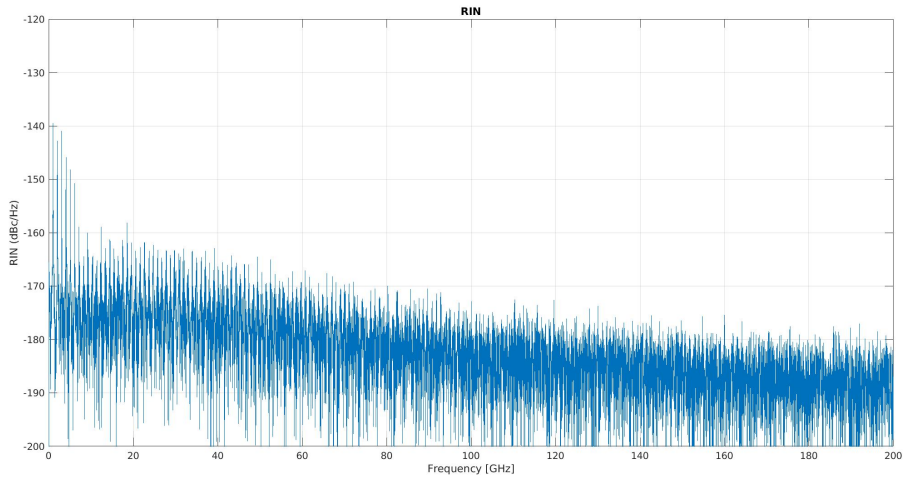

Figure 3.25: RIN spectrum $\epsilon = 0.7$.

Figures 3.26, 3.27 and 3.28 show the simulation's results with $\epsilon = 1$ for the modal intensity and RIN spectrum.

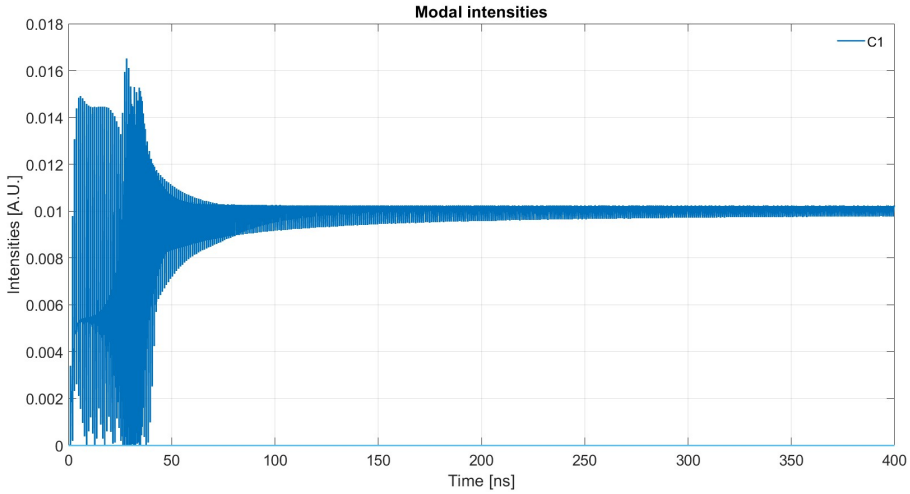

Figure 3.26: Modal intensity $\epsilon = 1$.

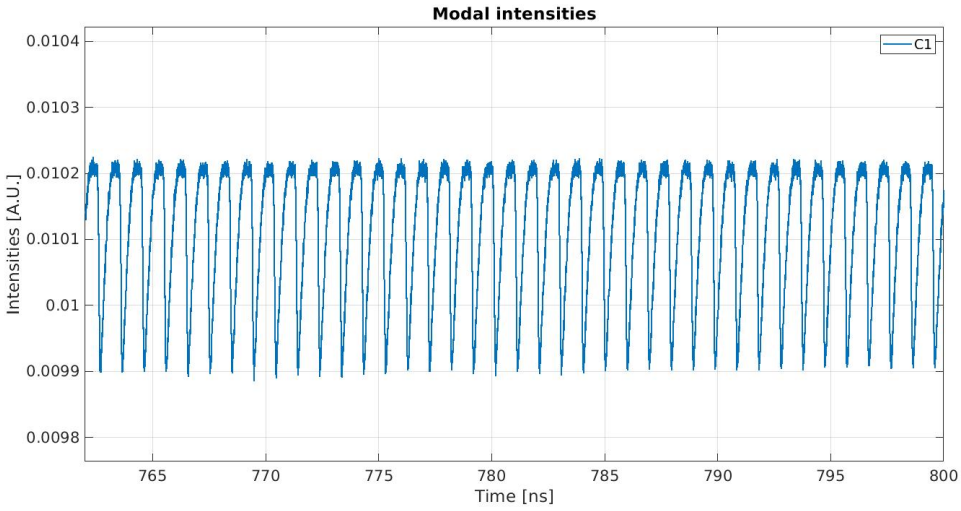

Figure 3.27: Modal intensity zoom at 770 ns $\epsilon = 1$.

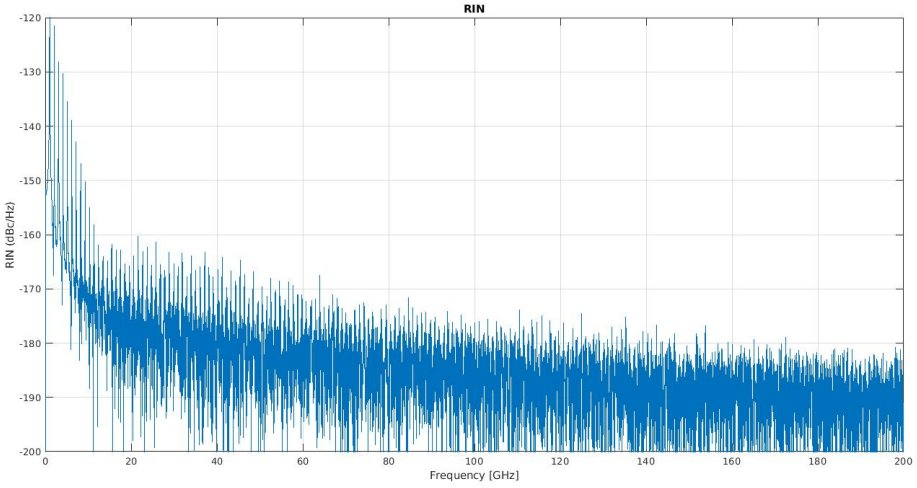

Figure 3.28: RIN spectrum $\epsilon = 1$.

Concluding, the increase the feedback level injected inside the system causes an increase of the RIN at low frequency with the appearance of peaks separated by the FSR of the external cavity.

Bifurcation Diagram

In order to evaluate the effect of the feedback on the system, bifurcation diagrams are plotted considering the variation of the power as a function of the feedback strength. Bifurcation diagram is useful to describe the VCSEL dynamics and its stability. Specifically, in cases where the VCSEL exhibits multiple modes, the bifurcation diagram can clarify which modes are most influenced by instability.

Bifurcation diagrams are obtained from the analysis of the time evolution of the modal intensities for different values of the feedback parameter.
When the modal intensity has reached the steady-state condition, its time evolution gives information about the stability of the system.
In order to obtain the bifurcation diagram, the relative maxima and minima of the photon density time evolution should be found and plotted.
A single point in the bifurcation diagram represents CW operation (Figure 3.29a), two points represent regular period-one oscillations (Figure 3.29b) and many points represent the chaotic behavior (Figure 3.29c).

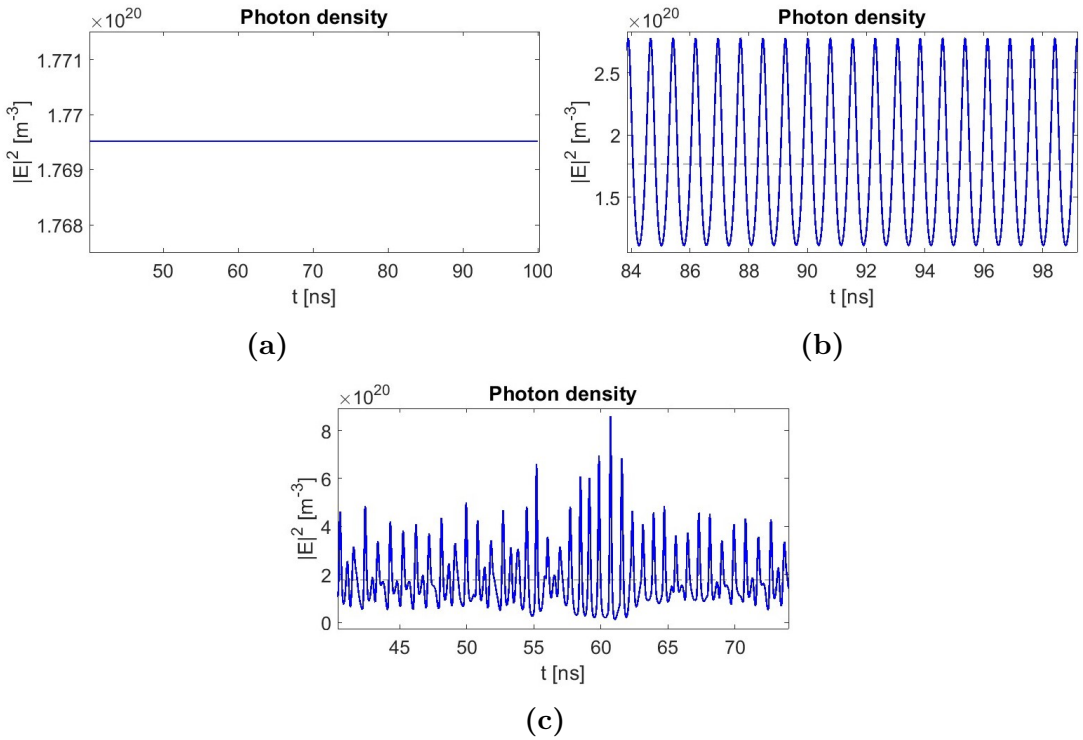

Figure 3.29: Time evolution of the photon density: CW solution (a), regular oscillations (b), chaotic behavior (c).

Figure 3.30 depicts the bifurcation diagram plotted considering the data shown in the previous section.
For each value of the feedback parameter the local maxima and minima of the modal intensity evolutions are plotted. Only the last ns of the temporal evolution are considered to avoid the transient state.

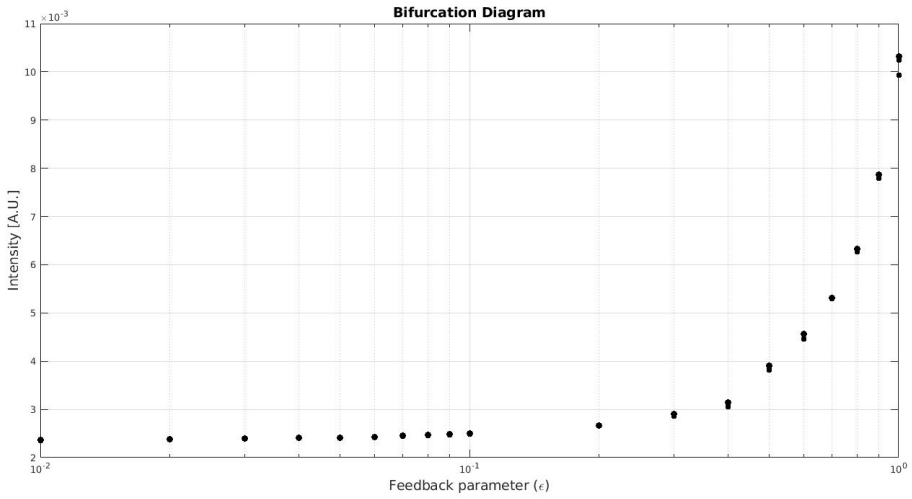

Figure 3.30: Bifurcation diagram.

According to Figure 3.30, the system exhibit a CW solution that differs for each of the feedback levels considered, since the bifurcation is not present in the graph. The amplitude of the oscillations of the modal intensities is not sufficient to enter in the second Regime described in Figure 3.2, the relaxation oscillations remains dumped, only the grow of the external cavity modes is observed.

Integrated RIN

Table 3.1 lists the evolution of the integrated RIN for different values of the attenuation parameter ϵ and for two different bandwidth values: 40 GHz and 5 GHz.
The trend of the Integrated RIN variation is illustrated in Figure 3.31.

Epsilon	Integrated RIN (40 GHz) [dBc/Hz]	Integrated RIN (5 GHz) [dBc/Hz]
0	-165.7264	-173.9684
0.01	-165.8577	-174.4116
0.02	-166.0013	-173.5837
0.03	-165.6071	-173.5198
0.04	-165.6557	-173.7567
0.05	-165.6323	-172.3745
0.06	-165.9908	-172.5034
0.07	-165.6967	-165.8121
0.08	-164.8759	-162.9030
0.09	-163.4616	-157.7332
0.1	-154.2921	-145.6216
0.2	-165.5516	-170.8341
0.3	-154.4743	-145.8013
0.4	-147.7510	-138.8529
0.5	-149.5513	-140.5738
0.6	-150.7029	-141.7400
0.7	-166.2190	-158.6617
0.8	-158.3964	-149.5157
0.9	-157.9679	-149.0556
1	-146.3291	-137.3837

Table 3.1: Integrated RIN.

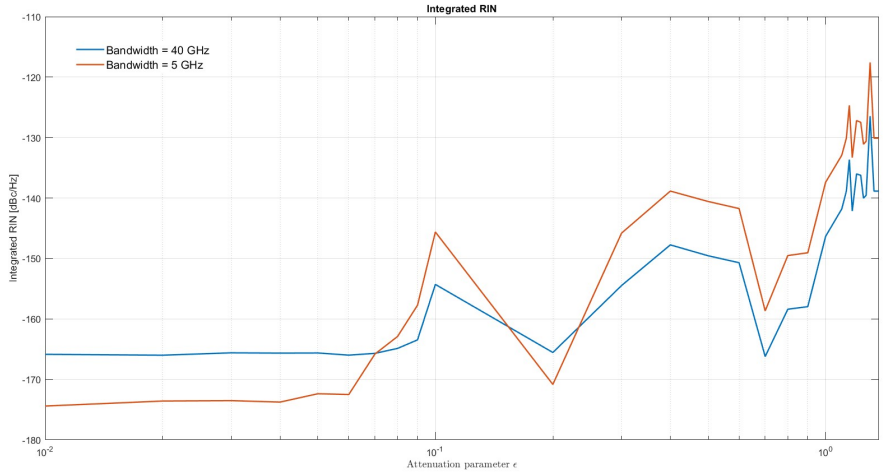

Figure 3.31: Integrated RIN as a function of attenuation parameter.

Until $\epsilon = 0.06$ the integrated RIN evaluated over a bandwidth of 40 GHz remains higher than the integrated RIN evaluated over a bandwidth of 5 GHz, and their values are approximately constant. When the feedback effect starts to influence the RIN spectra at low frequency, the value of the integrated RIN evaluated over a bandwidth of 40 GHz becomes lower than the integrated RIN evaluated over a bandwidth of 5 GHz.
The integrated RIN evolution as a function of the attenuation parameter presents some relative maxima in correspondence of $\epsilon = 0.1$, $\epsilon = 0.4$ and $\epsilon = 1.3$.

Chapter 4

Model Validation

The aim of this chapter is to test the validity of the model by comparing its results with those obtained using well tested approaches to describe semiconductor lasers subject to optical feedback.

The first test concerns the reproduction of the results obtained and published in the paper: *"Effects of Optical Feedback on Static and Dynamic Characteristics of Vertical-Cavity Surface-Emitting Lasers"* by Joanne Y. Law and Govind P. Agrawal.

The second test concerns the reproduction of the results of the more basic Lang-Kobayashi model under very simplifying hypotheses.

4.1 Comparison with another model for a multimode VCSEL subject to optical feedback

The objective is to validate both the model and the numerical code adopted to perform the simulations reported in the previous chapter by qualitatively reproducing the results in the paper titled *"Effects of Optical Feedback on Static and Dynamic Characteristics of Vertical-Cavity Surface-Emitting Lasers"* by Joanne Y. Law and Govind P. Agrawal, and to achieve comparable results.
A perfect match between the results obtained with the VCSEL model and those reported in the article is not possible, as the equations employed in the two cases differ slightly. In particular, the interference terms associated with modes competition are not properly taken into account in the Agrawal' model that thus results less accurate to describe multimode VCSEL operation.

The model used in the paper consist in the resolution of the following rate equations:

$$\frac{dE_i}{dt} = \frac{1}{2}[(1 - i\alpha)G_i(t) - \gamma_i]E_i + \sum_{m=1}^{M} k_m E_i(t - m\tau)e^{im\omega_i\tau} \tag{4.1}$$

Where G_i is the gain for the i-th mode [9].

$$\frac{\partial N}{\partial t} = D\nabla_T^2 N + \frac{J(r,\phi)}{qd} - \frac{N}{\tau_e} - BN^2 - \frac{1}{d}\sum_{i=i}^{n_{modes}} G_{local}|E_i(t)|^2|\psi_i(r,\phi)|^2 \tag{4.2}$$

In the previous equation, $G_{local} = \sigma(N - N_T)$ is the local gain defined in the small-signal regime, N is the local carrier density and N_T is the carrier density at transparency [9].

Another difference consists in the fact that the model described in the paper includes the effect of multiple round-trips of the optical feedback within the external cavity. Specifically, in the Equation 4.1, k_m represents the feedback parameter for the i_{th} mode after m external cavity round-trips, with M being the total number of round-trips included in the model. This is expected to not introduce qualitative changes in the system behavior with respect to the case of $m = 1$ that corresponds to our model [8].

Table 4.1 lists the parameters that characterize the device simulated in the paper.

Parameters	Values
Laser cavity length	$2\,\mu m$
Diffusion constant	$30\,cm^2/s$
Carrier lifetime (τ_e)	$5\,ns$
Refractive index (GaAs)	3.4
Emission wavelength	$895\,nm$
Carrier density at transparency (N_T)	$2.2 \times 10^{24}\,m^{-3}$
Linewidth enhancement factor (α)	3
Mirror reflectivity	0.995
Internal losses (α_i)	$2{,}000\,m^-1$
Confinement factor	0.012
Bias current	$2\ I_{th}$
Volume of the active region	$3.01 \times 10^{-19}\,m^3$
Differential gain coefficient $\cdot\ v_g$	$1.714 \times 10^{-12}\,m^3/s$
External cavity length	$10\,cm$

Table 4.1: Simulation parameters.

The main differences comparing Table 4.1 to the CISCO parameters discussed in the previous chapter lie in three parameters: the linewidth enhancement factor, which was set to 1 in the CISCO parameters but is set to 3 in the current analysis. The G_N factor, representing the product of the differential gain coefficient and the group velocity that in the current analysis is 4.5 times smaller than the value specified by CISCO; and the carrier lifetime that is 5 times the value used in the CISCO analysis.

We observe that we did not manage to retrieve all the input parameters required by our model from the paper. In order to complete the simulations, the missing values are taken from CISCO parameters. Table 4.2 lists the missing values taken from CISCO data.

Parameters	Values
Internal quantum efficiency (η_i)	0.76
Gain compression factor ϵ	$1.71 \times 10^{-23}\,\mathrm{m}^3$
Refractive index of the fiber n_f	1.45

Table 4.2: Parameters taken from Table 2.1.

The current profile used to bias the simulated device is assumed to be super-Gaussian as in our model, even if it's not specified in the paper.
In the paper's simulations, the bias current is set to twice the threshold current. To determine the threshold current, a PI characteristic is plotted without feedback and it is reported in Figure 4.1. The threshold current is 0.7 mA.

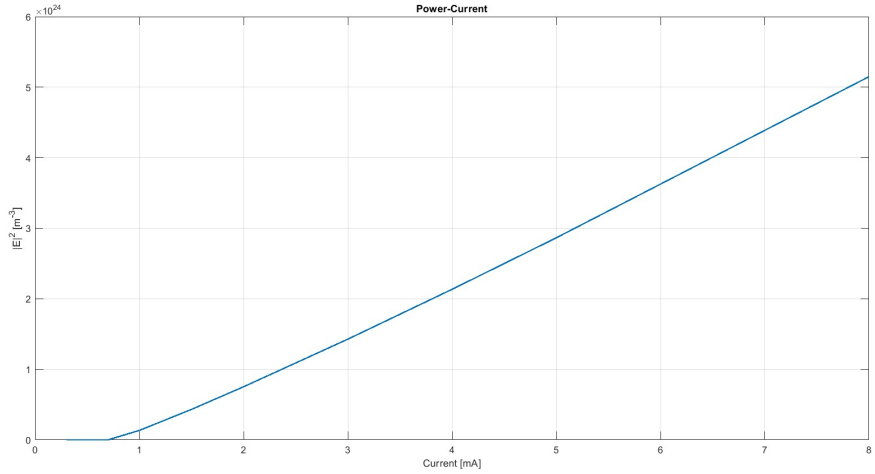

Figure 4.1: PI characteristic.

4.1.1 Single mode analysis

As a first analysis, only the fundamental mode is considered (mode C_1).
The threshold current obtained from the PI characteristic is 0.7 mA. Setting the bias current to twice this threshold value produces Figure 4.2, which shows the bifurcation diagram obtained from simulating the device using VCSEL code with a bias current of 1.4 mA. The feedback parameter k varies from 5×10^{-5} to 8×10^{-4}.

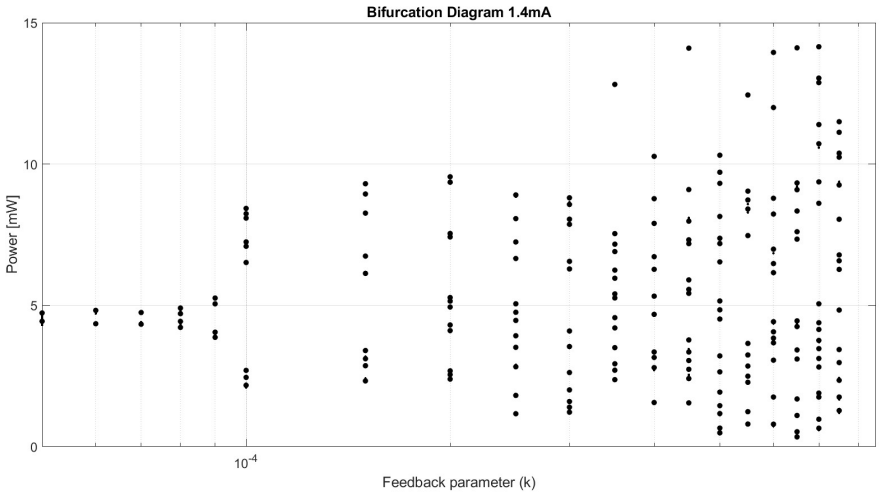

Figure 4.2: Bifurcation Diagram obtained from the simulation I = 1.4 mA.

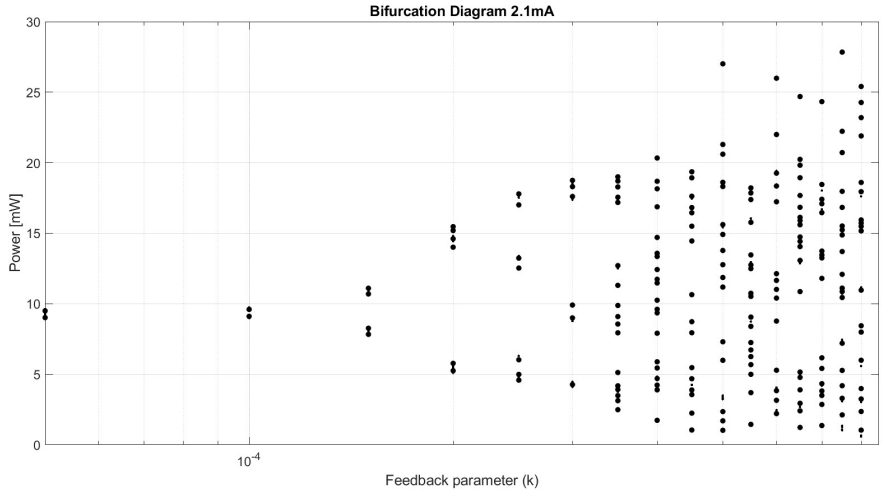

Figure 4.3: Bifurcation Diagram obtained from the simulation I = 2.1 mA.

Figure 4.3 presents the bifurcation diagram obtained with a bias current three times the threshold value. The bifurcation diagram in Figure 4.3 reproduces better the diagram of the paper (reported in Figure 4.4), in terms of critical feedback parameter and individuation of different working Regimes.

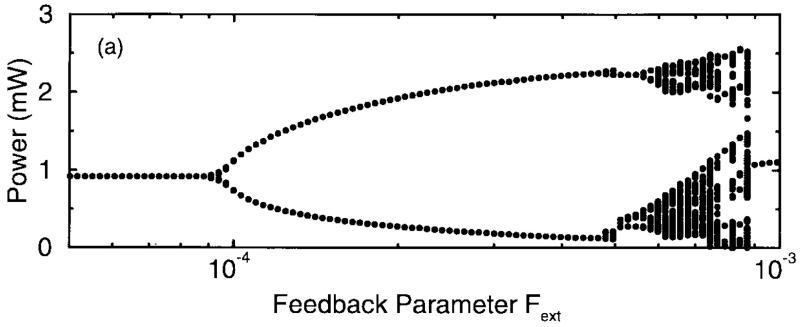

Figure 4.4: Bifurcation diagram taken from the paper [9].

The critical feedback parameter observed in Figure 4.3 is very close to that obtained in the paper results. The ranges of k that define the boundaries between the three regions of the diagram are instead more different. However, the three regimes can be identified:

- for $\kappa < 1 \times 10^{-4}$ the system exhibits a stable CW solution (Figure 4.5a);
- for $1 \times 10^{-4} < \kappa < 2 \times 10^{-4}$ the system oscillate regularly due to undamped relaxation oscillations (Figure 4.5b);
- for $\kappa > 2 \times 10^{-4}$ the chaotic regime starts (Figure 4.5c).

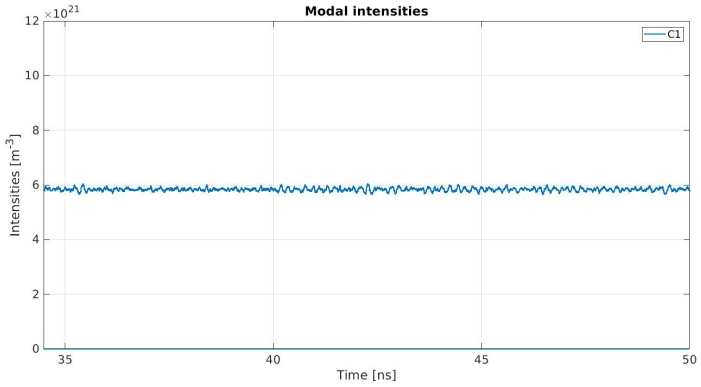

(a) $k = 5 \times 10^{-5}$.

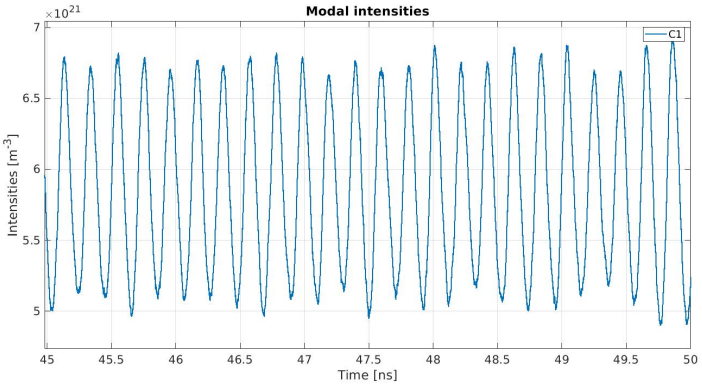

(b) $k = 1.5 \times 10^{-4}$.

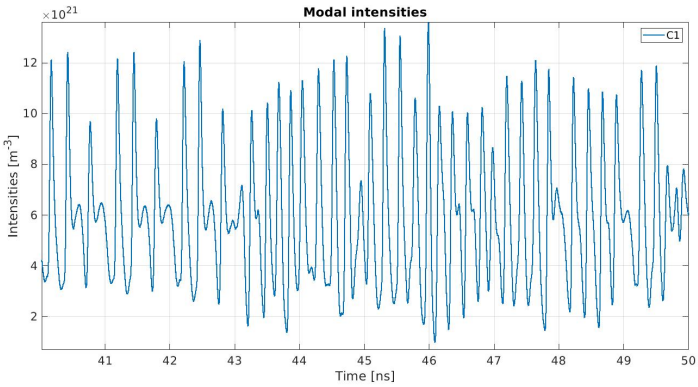

(c) $k = 3.5 \times 10^{-4}$.

Figure 4.5: CW state (a), regular oscillations (b), chaotic regime (c).

4.1.2 Two mode analysis

It is possible to extend the analysis considering two transverse mode. The value of the bias current used influences the modal amplitudes, and as a consequence, different bifurcation diagrams can be obtained using different bias current even if all the other parameters are left unchanged. In order to compare bifurcation diagrams for different propagating modes, the same bias current should be used. Two configurations are compared: in the first one the two propagating modes have a small spatial overlap (modes C_2 and C_3, Figure 4.6). In the second configuration, the spatial overlap between the two modes is much higher because the mode considered are C_2 and C_4 (Figure 4.7).

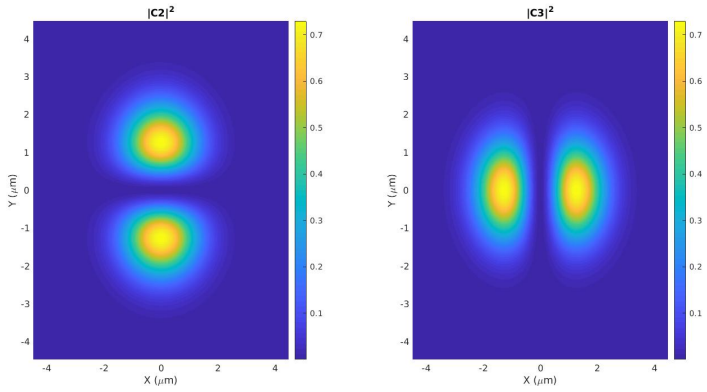

Figure 4.6: Modes C_2 and C_3.

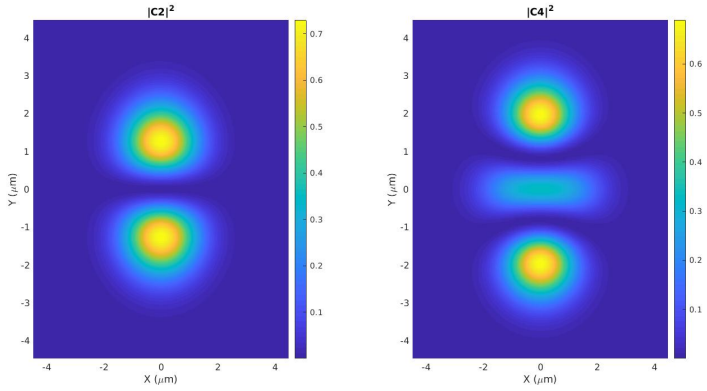

Figure 4.7: Modes C_2 and C_4.

In order to choose a proper current value for which C_2, C_3 and C_4 are on, we

rely on the study of the evolution of the modal intensities for a current sweep as reported in Figure 4.8.

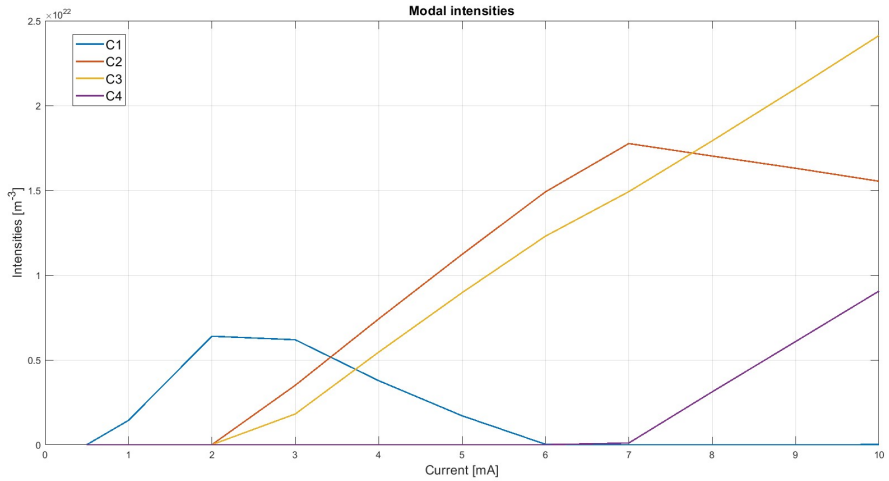

Figure 4.8: Modal intensity evolution.

The chosen current value is 7.3 mA, at which all three modes are active. Bifurcation diagrams for modes C_2 and C_3 and for modes modes C_2 and C_4 are reported respectively in Figures 4.9 and 4.10.

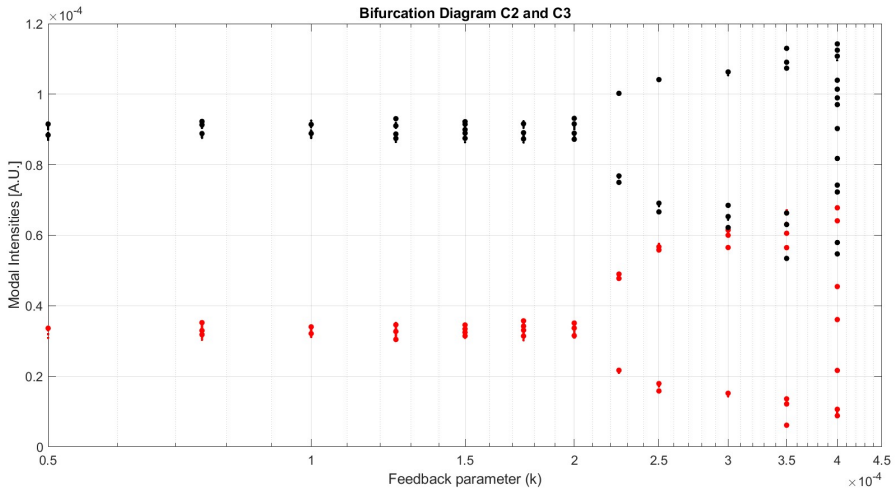

Figure 4.9: Bifurcation diagrams for modes C_2 (black dots) and C_3 (red dots).

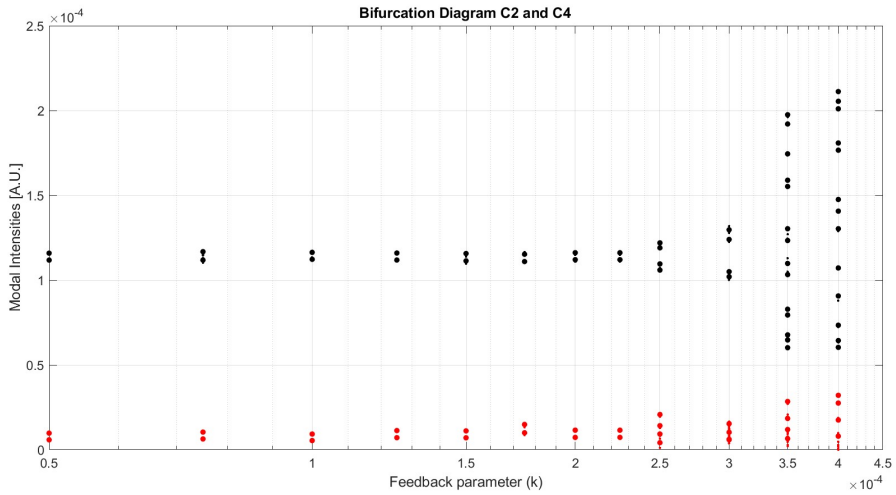

Figure 4.10: Bifurcation diagrams for modes C_2 (black dots) and C_4 (red dots).

Comparing the bifurcation diagrams obtained, it is evident that the critical feedback parameter is placed at higher value in the case of the two modes with the higher spatial overlap.
$\kappa_c = 2 \times 10^{-4}$ for the C_2C_3 configuration and $\kappa_c = 2.5 \times 10^{-4}$ for the C_2C_4 configuration.
In agreement with the results reported in the paper, due to strong coupling between the two modes through SHB, self-pulsations and onset of chaos occur at much higher feedback values [9]. We observe that a more satisfactory explanation of this phenomenon would deserve a further investigation.

Concluding, despite the differences between our model and the Agrawal's one, the MATLAB code developed by the supervisor research group is able to reproduce correctly the expected operating regimes of the VCSEL subjected to optical feedback.

4.2 Comparison with the standard Lang-Kobayashi approach

In this section, an analysis of a free-running laser is conducted using both the VCSEL code and another MATLAB code that implements the Lang-Kobayashi equations that describe a standard semiconductor laser subject to optical feedback [7]. The comparison can be done under the application of simplifying hypothesis listed in the following.

The differential equations for the modal amplitudes of the electric field and carrier density implemented in our multimode VCSEL model are reported in Equations 2.8 and 2.4.
The classical Lang-Kobayashi equations can be obtained starting from the VCSEL ones applying the simplified hypothesis of spatial uniform carriers density and electric field profile, negligible carriers diffusion, negligible gain compression factor and uniform pump profile.

The Lang-Kobayashi equations [7] are reported in the following.

$$\frac{dE(t)}{dt} = -\frac{1+i\alpha}{2\tau_p}E(t) + \frac{\Gamma G_N(1+i\alpha)}{2}E(t)[N(t)-N_0] \tag{4.3}$$

$$\frac{dN(t)}{dt} = \frac{\eta_i I_k}{eV} - \frac{N(t)}{\tau_e} - G_N|E(\rho,\phi,t)|^2[N(t)-N_0] \tag{4.4}$$

The quantities used for comparing the two codes include the threshold current and threshold carrier density, as listed in Table 4.3, while the relaxation oscillation frequency and PI characteristics are presented in Figures 4.13 and 4.14.
In order to verify the consistency between the two descriptions, the VCSEL code is executed assuming a Gaussian distribution of the electric field amplitude, carriers density and current (single mode approximation) to better match the VCSEL geometry.

	LK model	Simplified VCSEL model
Threshold current (I_{bias} value)	0.4 mA	0.6 mA
Threshold carrier density mean value	$2.965 \times 10^{24}\,\mathrm{m}^{-3}$	$2.537 \times 10^{24}\,\mathrm{m}^{-3}$
Threshold carrier density peak value	$2.965 \times 10^{24}\,\mathrm{m}^{-3}$	$5.110 \times 10^{24}\,\mathrm{m}^{-3}$

Table 4.3: Threshold current and carrier density for the VCSEL model.

We observe that the mean value of the carriers density, reported in Table 4.3 for the VCSEL code, is an average taken over the spatial distribution of the carriers

evaluated at the threshold current.

Figures 4.11 and 4.12 report the time evolution of the carriers density amplitude for current value set to 8 mA.

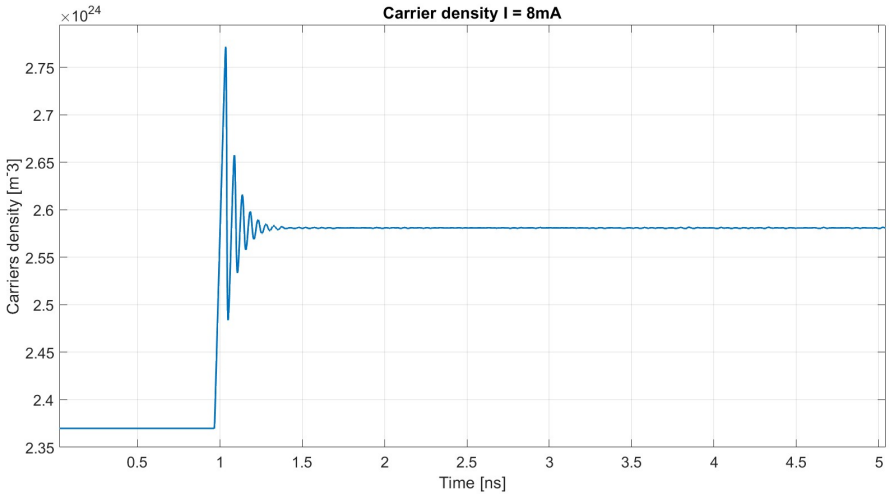

Figure 4.11: Time evolution of the carriers density: VCSEL model with simplifying hypothesis.

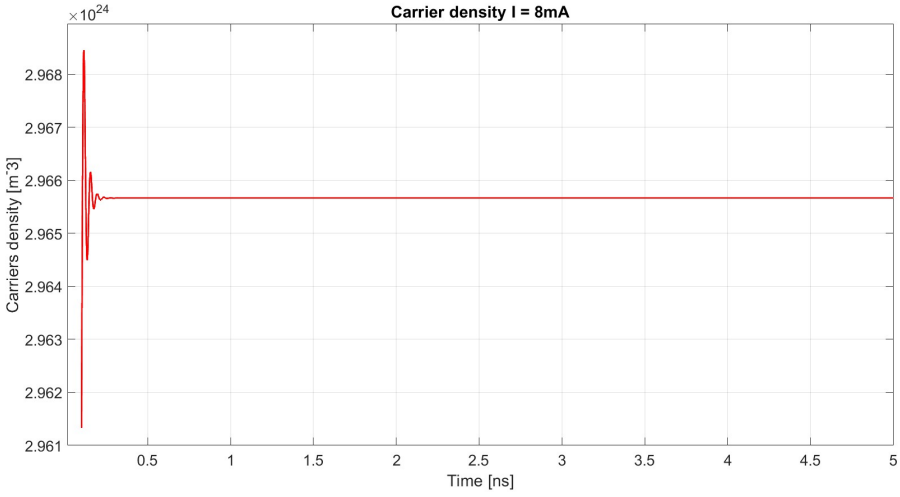

Figure 4.12: Time evolution of the carriers density: LK model.

Figures 4.13 and 4.14 show the comparison between the PI characteristics and the relaxation oscillation frequency evaluated using the two different approaches.

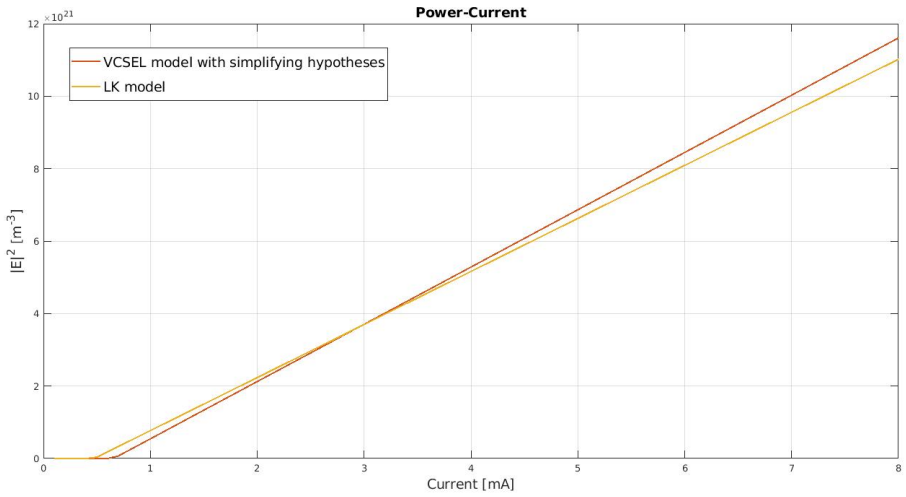

Figure 4.13: Power-Current characteristic.

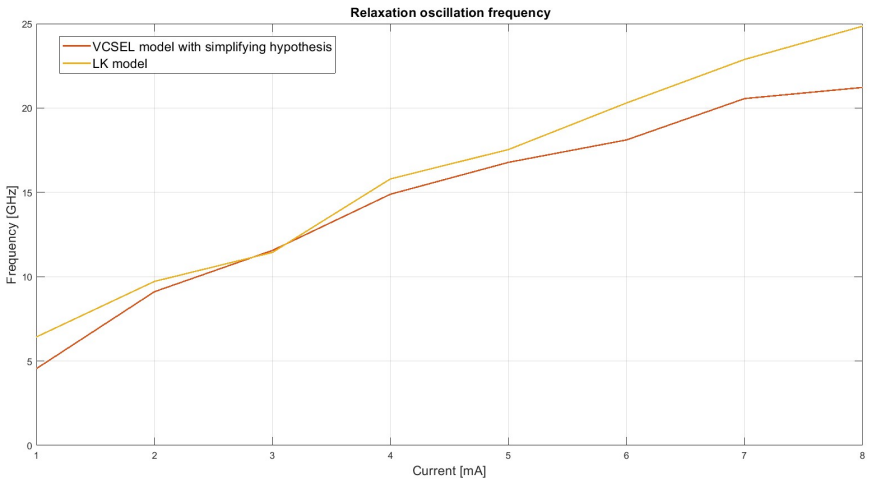

Figure 4.14: Relaxation oscillation frequency for different bias current.

The relaxation oscillation frequency values are obtained plotting RIN spectra and considering the frequency of the smooth peak for each current value.

The results obtained using the LK and VCSEL simplified approach are thus in good qualitative agreement. We observe in fact that the code used for the VCSEL simulation in the previous chapter has been developed to simulate multimode dynamics in presence of a spatially non uniform current profile. The single mode

simulations presented in this section were performed using a gaussian electric field, carriers density and current profile.
In the LK code, instead, the working hypothesis are uniform carriers profile and uniform injected current and electric field profile.
The different starting hypothesis may explain the observed differences between the results shown in Figures 4.11, 4.12, 4.13 and 4.14.
For example the integral of the gaussian current distribution leads to a smaller overall injected current with respect to a uniform current distribution for the same value of I_{bias}.

Appendix A

Modal rate equations

A.1 Carriers equation

$$N_k(\rho,\phi,t) = \sum_k N_k(t) B_k(\rho,\phi)$$

$$\frac{dN(\rho,\phi,t)}{dt} = \frac{\eta_i I(\rho,\phi,t)}{eV} - \frac{N(\rho,\phi,t)}{\tau_e} - \frac{n_g^2 \epsilon_0 G_N}{2\hbar\omega_0}[N(\rho,\phi,t) - N_0]\frac{|E(\rho,\phi,t)|^2}{1+\epsilon N_p(\rho,\phi,t)} + D\nabla_\perp^2 N(\rho,\phi,t)$$

Projecting $N(\rho,\phi,t)$ on the $B_k(\rho,\phi)$ mode, remembering that B_k is a real base ($B_k^*(\rho,\phi) = B_k(\rho,\phi)$)

$$N_k(t) = \int_0^\infty \int_0^{2\pi} N(\rho,\phi,t) B_k^*(\rho,\phi)\rho d\rho d\phi = \int_0^\infty \int_0^{2\pi} N(\rho,\phi,t) B_k(\rho,\phi)\rho d\rho d\phi$$

Also the current can be projected on the same modal base

$$I_k(t) = \int_0^\infty \int_0^{2\pi} I(\rho,\phi,t) B_k^*(\rho,\phi)\rho d\rho d\phi = \int_0^\infty \int_0^{2\pi} I(\rho,\phi,t) B_k(\rho,\phi)\rho d\rho d\phi$$

- L.H.S.:

$$\int_0^\infty \int_0^{2\pi} \left(\frac{dN(\rho,\phi,t)}{dt}\right) B_k(\rho,\phi)\rho d\rho d\phi = \frac{d}{dt} N_k(t)$$

- R.H.S.:

$$\int_0^\infty \int_0^{2\pi} \left(\frac{\eta_i I(\rho,\phi,t)}{eV} - \frac{N(\rho,\phi,t)}{\tau_e}\right) B_k(\rho,\phi)\rho d\rho d\phi = \frac{\eta_i I_k(t)}{eV} - \frac{N_k(t)}{\tau_e}$$

$$\int_0^\infty \int_0^{2\pi} \frac{n_g^2 \epsilon_0 G_N}{2\hbar\omega_0}[N(\rho,\phi,t) - N_0]\frac{|E(\rho,\phi,t)|^2}{1+\epsilon N_p(\rho,\phi,t)}\rho d\rho d\phi = \frac{n_g^2 \epsilon_0 G_N}{2\hbar\omega_0} g_k(t)$$

$$\int_0^\infty \int_0^{2\pi} D(\nabla_\perp^2 N(\rho,\phi,t)) B_k(\rho,\phi)\rho d\rho d\phi =$$

$$= D \int_0^\infty \int_0^{2\pi} B_k(\rho,\phi) \left[\nabla_\perp^2 \left(\sum_n N_n(t) B_n(\rho,\phi) \right) \right] \rho d\rho d\phi =$$

$$= D \int_0^\infty \int_0^{2\pi} B_k(\rho,\phi) \left[\sum_n N_n(t) \left(\nabla_\perp^2 B_n(\rho,\phi) \right) \right] \rho d\rho d\phi$$

For the property written in the supplementary of the paper [2], it is possible to write

$$\nabla_\perp^2 B_n(\rho,\phi) = 4[\rho^2 - (2\rho + |m| + 1)] B_n(\rho,\phi)$$

With $2\rho + |m| + 1 = q_n$.

$$\int_0^\infty \int_0^{2\pi} \left[D\nabla_\perp^2 N(\rho,\phi,t) \right] B_k(\rho,\phi) \rho d\rho d\phi =$$

$$= D \int_0^\infty \int_0^{2\pi} \left[\sum_n N_n(t) 4(\rho^2 - (2\rho + |m| + 1)) B_n(\rho,\phi) \right] B_k(\rho,\phi) \rho d\rho d\phi =$$

$$= 4D \sum_n N_n(t) \int_0^\infty \int_0^{2\pi} (\rho^2 B_n(\rho,\phi) B_k(\rho,\phi)) - 4D \sum_n N_n(t) \int_0^\infty \int_0^{2\pi} q_n B_n(\rho,\phi) B_k(\rho,\phi) \rho d\rho d\phi =$$

$$= d_k(t) - 4D \sum_n N_n(t) q_n \int_0^\infty \int_0^{2\pi} B_n(\rho,\phi) B_k(\rho,\phi) \rho d\rho d\phi =$$

With $\int_0^\infty \int_0^{2\pi} B_n(\rho,\phi) B_k(\rho,\phi) \rho d\rho d\phi = \delta_{nk}$,

$$= d_k(t) - 4D q_k N_k(t)$$

The complete equation is

$$\frac{d}{dt} N_k(t) = \frac{\eta_i I_k(t)}{eV} - \frac{N_k(t)}{\tau_e} + \frac{n_g^2 \epsilon_0 G_N}{2\hbar\omega_0} g_k(t) + d_k(t) - 4D q_k N_k(t)$$

A.2 Electric field equation

$$\frac{d\tilde{E}(\rho,\phi,t)}{dt} = -\frac{(1+i\alpha))}{2\tau_p}\tilde{E}(\rho,\phi,t) + \frac{\Gamma G_N(1+i\alpha)}{2}\frac{\tilde{E}(\rho,\phi,t)}{1+\epsilon N_p(\rho,\phi,t)}[N(\rho,\phi,t)-N_0] + S_{sp}(\rho,\phi,t)$$

Projecting $\tilde{E}(\rho,\phi,t)$ on $C_m(\rho,\phi)$ modes

$$\tilde{E}_m(t) = \int_0^\infty \int_0^{2\pi} \tilde{E}(\rho,\phi,t)C_m^*(\rho,\phi)\rho d\rho d\phi$$

- L.H.S.:

$$\int_0^\infty \int_0^{2\pi} \left(\frac{d}{dt}\tilde{E}(\rho,\phi,t)\right) C_m(\rho,\phi)\rho d\rho d\phi = \frac{d}{dt}\int_0^\infty \int_0^{2\pi} \tilde{E}(\rho,\phi,t)C_m(\rho,\phi)\rho d\rho d\phi = \frac{d\tilde{E}_m(t)}{dt}$$

- R.H.S.:

$$-\int_0^\infty \int_0^{2\pi} \frac{(1+i\alpha)}{2\tau_p}\tilde{E}(\rho,\phi,t)C_m(\rho,\phi)\rho d\rho d\phi = -\frac{(1+i\alpha)}{2\tau_p}\tilde{E}_m(t)$$

$$\int_0^\infty \int_0^{2\pi} \frac{\Gamma G_N(1+i\alpha)}{2}\frac{\tilde{E}(\rho,\phi,t)}{1+\epsilon N_p(\rho,\phi,t)}[N(\rho,\phi,t)-N_0]\rho d\rho d\phi = \frac{\Gamma G_N(1+i\alpha)}{2}\tilde{f_m}(t)$$

$$\int_0^\infty \int_0^{2\pi} \tilde{S}_{sp}(\rho,\phi,t)C_m(\rho,\phi)\rho d\rho d\phi = \tilde{S_{sp}}(t)$$

The final equation is

$$\frac{d\tilde{E_m}}{dt} = -\frac{(1+i\alpha)}{2\tau_p}\tilde{E_m}(t) + \frac{\Gamma G_N(1+i\alpha)}{2}\tilde{f_m}(t) + \tilde{S}_{sp}(t)$$

Substituting $E_m(t) = \tilde{E}_m(t)e^{i\omega_m t}$ and assuming that ω_m are all equal

$$\frac{d\tilde{E_m}(t)}{dt} = e^{-i\omega_m t}\frac{dE_m(t)}{dt} + e^{-i\omega_m t}(-i\omega_m)E_m(t) = -\frac{(1+i\alpha)}{2\tau_p}e^{-i\omega_m t}E_m(t) + \frac{\Gamma G_N(1+i\alpha)}{2}\tilde{f_m}(t) + \tilde{S}_{sp}(t)$$

It is possible to write

$$\frac{dE_m(t)}{dt} = \left(-\frac{(1+i\alpha)}{2\tau_p} + i\omega_m\right)E_m(t) + \frac{\Gamma G_N(1+i\alpha)}{2}e^{i\omega_m t}\tilde{f_m}(t) + e^{i\omega_m t}\tilde{S}_{sp}(t)$$

Considering the term $\tilde{f_m}(t)$

$$e^{i\omega_m t}\tilde{f_m}(t) = e^{i\omega_m t}\int_0^\infty \int_0^{2\pi} \frac{\tilde{E}(\rho,\phi,t)}{1+\epsilon N_p(\rho,\phi,t)}[N(\rho,\phi,t)-N_0]\rho d\rho d\phi =$$

$$= \int_0^{\infty} \int_0^{2\pi} e^{i\omega_m t} \frac{\left(\sum_m \tilde{E}_m(t) C_m(\rho,\phi)\right)}{1+\epsilon N_p(\rho,\phi,t)} [N(\rho,\phi,t) - N_0] \rho d\rho d\phi =$$

$$= \int_0^{\infty} \int_0^{2\pi} e^{i\omega_m t} \frac{(\sum_m E_m(t) e^{-i\omega_m t} C_m(\rho,\phi))}{1+\epsilon N_p(\rho,\phi,t)} [N(\rho,\phi,t) - N_0] \rho d\rho d\phi =$$

$$\frac{dE_m(t)}{dt} = \left(-\frac{(1+i\alpha)}{2\tau_p} + i\omega_m \right) E_m(t) + \frac{\Gamma G_N (1+i\alpha)}{2} f_m(t) + S_{sp}(t)$$

Taking into account that

- Different mode families exist, they have different thresholds and different detuning;
- Due to the elliptical aperture, also modes belonging to the same family can have different thresholds and different detuning.

Assuming that ω_m are all different and that they have different τ_p,

$$\frac{dE_m(t)}{dt} = \left(-\frac{(1+i\alpha)}{2\tau_{p,m}} + i\omega_m \right) E_m(t) + \frac{\Gamma G_N (1+i\alpha)}{2} f_m(t) + S_{sp}(t)$$

Appendix B

Stability Analysis

In this section, the Lang-Kobayashi model introduced earlier is applied to highlight the dynamics expected when a semiconductor laser is subjected to optical feedback. There will be some differences with the VCSEL model because the LK model accounts for only a single mode, whereas the VCSEL description includes the analysis of multiple transverse modes.
Using the LK code, bifurcation diagrams can be obtained and a stability analysis can be conducted to find out the instability boundaries of the system and one might think to extend these techniques to the more complex model of a multimode VCSELs subjected to optical feedback presented in Chapter 2.

The first step for the application of the stability analysis is to find out the CW (Continuous Wave) solutions of the LASER, which are monochromatic solutions.
The second step involves determining the instability boundaries of these CW solutions, which means identifying the current values at which the CW solution becomes unstable. For the VCSEL case, the stationary solution is represented by a transverse mode because of optical feedback.
Once the stationary solutions are evaluated, the linear stability analysis can be applied. It consists in perturbing the CW solution (all the dynamical variable are perturbed, i.e. the electric field and the carriers) and writing the equation for the temporal evolution of the perturbations [8]. In doing so, and neglecting the terms of order higher than one in the perturbations, the dynamical system is linearized and standard technique for the resolution of dynamical systems are applied.
One of these methods consists in finding the eigenvalues of the matrix written from the system of equations. The derived Jacobian matrix contains elements depending on the stationary solutions (electric field and carriers evaluated at a certain frequency). From the diagonalization of the Jacobian matrix, the complex eigenvalues can be evaluated. The real and the imaginary part of the eigenvalues give information on the temporal evolution of the perturbations.

If there is any eigenvalue with positive real part, than the stationary solution is unstable because the perturbation increases exponentially.
The eigenvalues depend on the matrix elements that depend on the systems parameters. The threshold condition depends on the current distribution.

Parameters used for the stability analysis are listed in Table B.1.

Parameter	Value	Parameter	Value
DBR reflectivity	0.98	R_{ext}	0.06
λ_0	850 nm	L_{ext}	0.3 m
N_0	$2.37 \times 10^{24}\,\mathrm{m}^{-3}$	Current	2 mA
n_r	3.4	n_{fiber}	1.45
α	3	V	$7 \times 10^{-19}\,\mathrm{m}^3$
G_N	$7.78 \times 10^{-12}\,\mathrm{m}^3\mathrm{s}^{-1}$	τ_p	3.24 ps
η_i	0.76	τ_e	0.92 ns
Γ	0.0666	Cavity length	1 µm

Table B.1: Parameters for stability analysis.

Stationary solution

Starting from parameters listed in Table B.1, the stationary solution can be evaluated.
The stationary value of the angular frequency ω_s can be found solving the transcendental equation B.1.

$$\omega_s = \omega_{sol} - (\frac{\kappa}{\tau_c}) \cdot \sqrt{1+\alpha^2} \cdot \sin(w_s \cdot \tau_{ext} + atan(\alpha)) \tag{B.1}$$

Where $\omega_{sol} = \frac{2\pi c}{\lambda_0}$.
Fixing the value of the feedback parameter ($\kappa = 7.8 \times 10^{-6}$), Equation B.1 can be solved graphically.

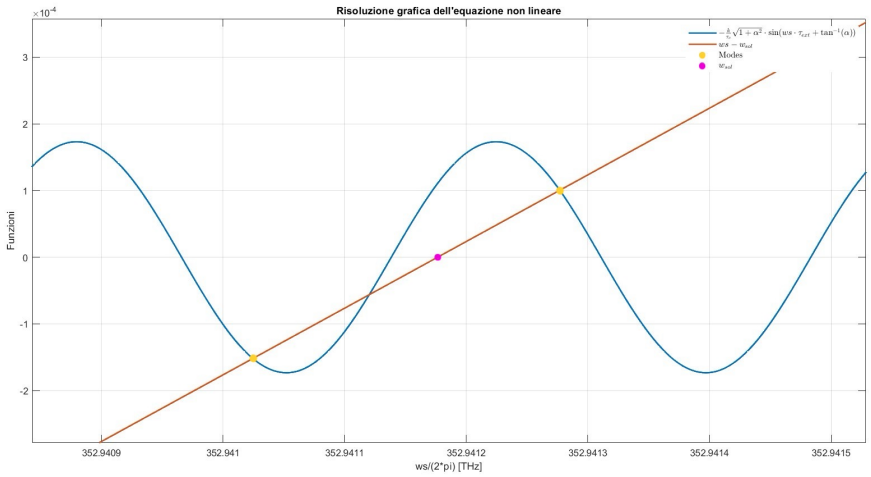

Figure B.1: Stationary solution for the angular frequency for $\kappa = 7.8 \times 10^{-6}$.

For $\kappa = 7.8 \times 10^{-6}$, there are three possible solutions for the angular frequency. These solutions correspond to either modes or anti-modes of the cavity, depending on whether the feedback and the field inside the cavity overlap in phase (mode) or in counter-phase (anti-mode). Modes are marked with yellow dots in Figure B.1, and the stationary solution is identified as the mode closest to the angular frequency of the free-running laser. The stationary angular frequency is found to be 352.941 THz.
The correctness of the stationary solution can be verified using the 'fzero' function in MATLAB.
The second method for validating the solution involves using the LK code with a feedback parameter that destabilizes the system by altering the stationary solution compared to that of a free-running laser. However, this is done such that the system remains within the first dynamical regime.
In order to evaluate the stationary value of the angular frequency, the optical spectrum is plotted taking into account the power emitted excluding the transient frame. The resulting peak is in correspondence of the frequency detuning of the stationary solution with respect to the ω_0 $(w_s - w_0)$.
The optical spectrum, within the evolution of the carriers density, photon density and RF spectrum are reported in Figure B.2.

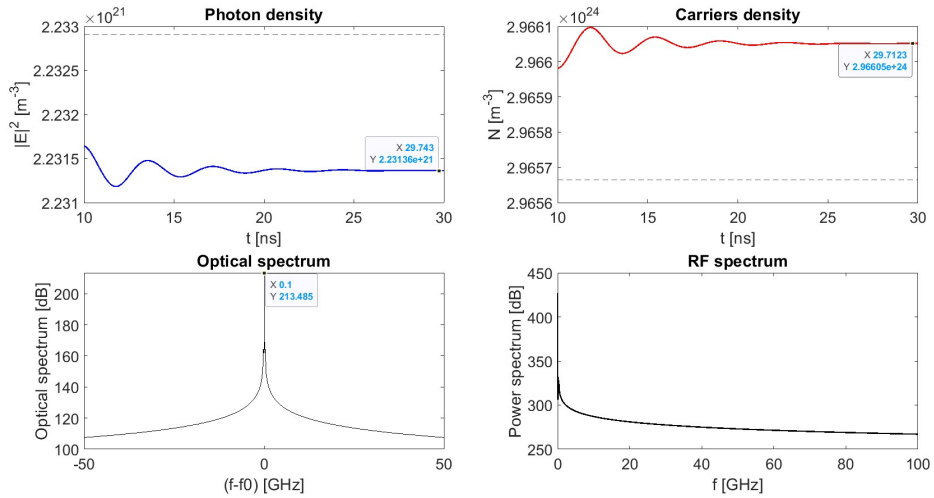

Figure B.2: LK solution for $\kappa = 7.8 \times 10^{-6}$.

Once the ω_s has been determined, also the stationary value of the square modulus of the electric field (I_s) and the stationary value of the carrier's density (N_s) can be evaluated respectively through Equations B.4 and B.2.

$$N_s = N_{sol} - \frac{\kappa}{\Re(\xi)\tau_c} cos(\omega_s \tau_{ext}) \tag{B.2}$$

Where N_{sol} is the value of the carrier density at threshold for the solitary laser, and it's evaluated through Equation B.3.

$$N_{sol} = N_0 + \frac{1}{\Gamma \tau_p G_n} \tag{B.3}$$

$$I_s = (\frac{\eta_i I}{qV} - \frac{N_s}{\tau_e}) \frac{1}{G_n(N_s - N_0)} \tag{B.4}$$

Values obtained from Equations B.2 and B.4 matches the results of the LK analysis reported in figure B.2.
Table B.2 listed the stationary solution obtained with the LK code and the one obtained through the stability analysis.

	LK code	Stability Analysis
$\frac{\omega_s - w_{sol}}{2\pi}$	0.1 GHz	0.1 GHz
N_s	2.966×10^{24}	2.966×10^{24}
I_s	2.231×10^{21}	2.227×10^{21}

Table B.2: Stationary solution evaluated through the LK code and stability analysis

Jacobian matrix definition

For fixed values of ω_s, I_s and N_s, the stability analysis can be implemented. Equations B.5 represent the system of equations obtained at the end of the derivation reported in Appendix B.

$$\begin{cases} \delta\dot{I}(t) = 2I_s\Re(\xi)\delta N(t) - \frac{\kappa}{\tau_c}[\delta I(t) - \delta I(t-\tau_{ext})]\cos(\omega_s\tau_{ext}) + \\ \qquad -2I_s\frac{\kappa}{\tau_c}[\delta\Phi(t) - \delta\Phi(t-\tau_{ext})]\sin(\omega_s\tau_{ext}) \\ \\ \delta\dot{\Phi}(t) = \Im(\xi)\delta N(t) - \frac{\kappa}{\tau_c}[\delta\Phi(t) - \delta\Phi(t-\tau_{ext})]\cos(\omega_s\tau_{ext}) + \\ \qquad -\frac{\kappa}{\tau_c}\frac{\delta I(t-\tau_{ext}) - \delta I(t)}{2I_s}\sin(\omega_s\tau_{ext}) \\ \\ \delta\dot{N}(t) = -\Gamma_N\delta N(t) - \frac{v_g g_n}{N_0}(N_s - N_0)\delta I(t) \end{cases} \tag{B.5}$$

In the frequency domain the system B.5 can be written as Equations B.6.

$$\begin{cases} i\tilde{\omega}\delta I(\tilde{\omega}) = -\frac{\kappa}{\tau_c}(1 - e^{-i\tilde{\omega}\tau_{ext}})\cos(\omega_s\tau_{ext})\delta I(\tilde{\omega}) + \\ \qquad -2I_s\frac{\kappa}{\tau_c}(1 - e^{-i\tilde{\omega}\tau_{ext}})\sin(\omega_s\tau_{ext})\delta\Phi(\tilde{\omega}) + 2I_s\Re(\xi)\delta N((\tilde{\omega})) \\ \\ i\tilde{\omega}\delta\Phi(\tilde{\omega}) = -\frac{\kappa}{\tau_c}\frac{(1-e^{-i\tilde{\omega}\tau_{ext}})}{2I_s}\sin(\omega_s\tau_{ext})\delta I(\tilde{\omega}) + \\ \qquad -\frac{\kappa}{\tau_c}(1 - e^{-i\tilde{\omega}\tau_{ext}})\cos(\omega_s\tau_{ext})\delta\Phi(\tilde{\omega}) + \Im(\xi)\delta N((\tilde{\omega})) \\ \\ i\tilde{\omega}\delta N(\tilde{\omega}) = -\frac{v_g g_n}{N_0}(N_s - N_0)\delta I(\tilde{\omega}) - \Gamma_N\delta N((\tilde{\omega})) \end{cases} \tag{B.6}$$

The Jacobian matrix can be derived from system B.6 in the form

$$\mathbf{M} = \begin{bmatrix} -\frac{\kappa}{\tau_c}(1 - e^{-i\tilde{\omega}\tau_{ext}})\cos(\omega_s\tau_{ext}) & -2I_s\frac{\kappa}{\tau_c}(1 - e^{-i\tilde{\omega}\tau_{ext}})\sin(\omega_s\tau_{ext}) & 2I_s\Re(\xi) \\ \\ -\frac{\kappa}{\tau_c}\frac{(1-e^{-i\tilde{\omega}\tau_{ext}})}{2I_s}\sin(\omega_s\tau_{ext}) & -\frac{\kappa}{\tau_c}(1 - e^{-i\tilde{\omega}\tau_{ext}})\cos(\omega_s\tau_{ext}) & \Im(\xi) \\ \\ -\frac{v_g g_n}{N_0}(N_s - N_0) & 0 & -\Gamma_N \end{bmatrix}$$

Where

$$\Gamma_N = \frac{1}{tau_e} + \frac{G_n N_0 I_s}{N_s} \tag{B.7}$$

$$\xi = \Gamma G_N\frac{(1 + i\alpha)}{2} \tag{B.8}$$

In order to evaluate the eigenvalues of the matrix M, the zero of the determinant (Equation B.9) should be found.

$$det(M - \lambda I) = 0 \tag{B.9}$$

In this analysis, the eigenvalues are expressed as $\lambda = i\tilde{\omega}$. This implies that an unstable CW solution will be associated with $\Im(i\tilde{\omega}) < 0$.
The purpose of the analysis is to understand how the $\Im(i\tilde{\omega})$ varies with the feedback coefficient κ.

Instability boundaries

In order to find out the instability boundaries, it is sufficient to impose that $\Im(i\tilde{\omega}) = 0$, which means supposing that $\tilde{\omega}$ is a real variable:

- when $\Im(i\tilde{\omega}) < 0$, the solution is unstable;
- when $\Im(i\tilde{\omega}) > 0$, the solution is stable;

By fixing the value of the external cavity length, it is possible to identify the κ values corresponding to the existence of a solution.
The instability boundaries are identified by the value of κ_{crit}, which corresponds to the transition from stable to periodic regime.

B.1 Mathematical derivation

In the following derivation, some approximations are applied:

- Single mode approximation,
- Negligible gain compression factor,
- Negligible diffusion,
- Constant current and constant carriers distribution. With this approximation, the electric field distribution also remains spatially constant.

The two equations that describe the evolution of the electric field and the carriers density are

$$\frac{dE(t)}{dt} = \left(-\frac{1}{2\tau_p}(1+i\alpha)\right)E(t) + \frac{\Gamma}{2}G_n(1+i\alpha)E(N-N_0) + \frac{\kappa}{\tau_c}E(t-\tau_{ext})e^{-i\omega_0\tau_{ext}}$$
$$\frac{dN(t)}{dt} = \frac{\eta_i I}{eV} - \frac{N}{\tau_e} - G_n(N-N_0)|E(t)|^2$$

Writing $E(t) = \rho(t)e^{i\phi(t)}$, the equation for the modulus and for the phase of the electric field can be obtained.

- LHS :
$$\frac{d\left[\rho(t)e^{i\phi(t)}\right]}{dt} = \frac{d\rho(t)}{dt}e^{i\phi(t)} + \rho(t)\frac{de^{i\phi(t)}}{dt}$$
- RHS :
$$\left(-\frac{1}{2\tau_p}(1+i\alpha)\right)\rho(t)e^{i\phi(t)} + \frac{\Gamma}{2}G_n(1+i\alpha)\rho(t)e^{i\phi(t)}[N-N_0] + \\ + \frac{\kappa}{\tau_c}\rho(t-\tau_{ext})e^{i\phi(t-\tau_{ext})}e^{-i\omega_0\tau_{ext}}$$

By separating modulus and phase, the result is:

- Modulus:
$$\frac{d\rho(t)}{dt}e^{i\phi(t)} = (-\frac{1}{2\tau_p} + \frac{\Gamma}{2}G_n[N-N_0]\Big)\rho(t)e^{i\phi(t)} + \frac{\kappa}{\tau_c}\rho(t-\tau_{ext})e^{i\phi(t-\tau_{ext})}e^{-i\omega_0\tau_{ext}}$$
$$\frac{d\rho(t)}{dt} = \left(-\frac{1}{2\tau_p} + \frac{\Gamma}{2}G_n[N-N_0]\right)\rho(t) + \frac{\kappa}{\tau_c}\rho(t-\tau_{ext})e^{i\phi(t-\tau_{ext})}e^{-i\omega_0\tau_{ext}}e^{i\phi(t)}$$
- Phase:
$$\rho(t)e^{i\phi(t)}\frac{d\phi(t)}{dt} = \left(\frac{\alpha}{2\tau_p} + \frac{\Gamma}{2}\,\mathrm{G_n}\,\alpha[N-N_0]\right)\rho(t)e^{i\phi(t)} + \frac{\kappa}{\tau_c}\rho(t-\tau_{ext})e^{i\phi(t-\tau_{ext})}e^{-i\omega_0\tau_{ext}}$$
$$\frac{d\phi(t)}{dt} = \frac{\alpha}{2\tau_p} + \frac{\Gamma}{2}G_n\alpha[N-N_0] + \frac{\kappa}{\tau_c}\frac{\rho(t-\tau_{ext})}{\rho(t)}e^{i\phi(t-\tau_{ext})}e^{-i\omega_0\tau_{ext}}e^{i\phi(t)}$$

Writing the exponential terms with the Euler's formula:

$$\frac{d\rho(t)}{dt} = \left(-\frac{1}{2\tau_p} + \frac{\Gamma}{2}G_n[N-N_0]\right)\rho(t) + \frac{\kappa}{\tau_c}\rho(t-\tau_{ext})\cos[\phi(t-\tau_{ext}) - \omega_0\tau_{ext} - \phi(t)]$$
$$\frac{d\Phi(t)}{dt} = \frac{\alpha}{2\tau_p} + \frac{\Gamma}{2}G_n\alpha[N-N_0] + \frac{\kappa}{\tau_c}\frac{\rho(t-\tau_{ext})}{\rho(t)}\sin[\phi(t-\tau_{ext}) - \omega_0\tau_{ext} - \phi(t)]$$

Since the cos is an even function $\cos(-x) = \cos(x)$ and the sin is an odd function $\sin(-x) = -\sin(x)$, the two equations can be written as

$$\frac{d\rho(t)}{dt} = \left(-\frac{1}{2\tau_p} + \frac{\Gamma}{2}G_n[N-N_0]\right)\rho(t) + \frac{\kappa}{\tau_c}\rho(t-\tau_{ext})\cos\left[\omega_0\tau_{ext} + \phi(t) - \phi(t-\tau_{ext})\right]$$
$$\frac{d\phi(t)}{dt} = \frac{\alpha}{2\tau_p} + \frac{\Gamma}{2}G_n\alpha[N-N_0] - \frac{\kappa}{\tau_c}\frac{\rho(t-\tau_{ext})}{\rho(t)}\sin\left[\omega_0\tau_{ext} + \phi(t) - \phi(t-\tau_{ext})\right]$$

Starting from these equations, the more general equations describing the stability analysis can be derived. The case under consideration is the Fabry-Perot configuration, in which

$$\gamma_L = \left(2L\frac{\partial\,\mathrm{Re}(\kappa(\omega,N))}{\partial\omega}\right)^{-1} = \frac{1}{\tau_{in}} = \frac{1}{\tau_c}$$

So $\phi_{\gamma L} = 0$ and $\rho_{\gamma L} = \frac{1}{\tau_{in}}$.
In order to obtain the more general Lang-Kobayashy equations, it is necessary substituting the two terms

$$\frac{1}{\tau_p} = \frac{\mathrm{v_g}\, g_N \Gamma}{2N_0}\,(N_{sol} - N_0) \qquad \text{and} \qquad G_N = \frac{\mathrm{v_g}\, g_n}{N_0}$$

$$\begin{aligned}\frac{d\rho(t)}{dt} =& \left(-\frac{v_g g_n \Gamma}{2N_0}(N_{sol} - N_0) + \frac{\Gamma}{2}\frac{v_g g_n}{N_0}[N - N_0]\right)\rho(t) + \\ &+ \frac{\kappa}{\tau_c}\rho(t-\tau_{ext})\cos[\omega_0\tau_{ext} + \phi(t) - \phi(t-\tau_{ext})] \\ \frac{d\rho(t)}{dt} =& \frac{v_g g_n \Gamma}{2N_0}(N - N_{sol})\rho(t) + \frac{\kappa}{\tau_c}\rho(t-\tau_{ext})\cos\left[\omega_0\tau_{ext} + \phi(t) - \phi(t-\tau_{ext})\right]\end{aligned}$$

In the equations, $\omega_0 = \omega_{sol}$ is the solitary laser frequency = 850 nm.

$$\begin{aligned}\frac{d\Phi(t)}{dt} =& \frac{\alpha v_g g_N \Gamma}{2N_0}(N_{sol} - N_0) + \frac{\Gamma}{2}\frac{v_g g_N}{N_0}\alpha(N - N_0) + \\ &- \frac{\kappa}{\tau_c}\frac{\rho(t-\tau_{ext})}{\rho(t)}\sin[\omega_0\tau_{ext} + \phi(t) - \phi(t-\tau_{ext})] \\ \frac{d\Phi(t)}{dt} =& \frac{\alpha v_g g_N \Gamma}{2N_0}(N - N_{sol}) - \frac{\kappa}{\tau_c}\frac{\rho(t-\tau_{ext})}{\rho(t)}\sin[\omega_0\tau_{ext} + \phi(t) - \phi(t-\tau_{ext})]\end{aligned}$$

These equations are formally equal to the Lang-Kobayashy ones. The linear gain model has been applied, in which

$$\xi = \frac{v_g g_n}{2N_0}\Gamma(1 + i\alpha)$$

ξ depends on ω_{sol} and N_{sol}, but the explicit dependence on N is eliminated.
Substituting ξ in the two equations for the modulus and phase

$$\begin{aligned}\frac{d\rho(t)}{dt} &= \mathrm{Re}[\xi](N(t) - N_{sol})\rho(t) + \kappa\rho_{\gamma_L}\rho(t-\tau_{ext})\cos\left[\omega_{sol}\tau_{ext} + \phi(t) - \phi(t-\tau_{ext}) + \phi_{\gamma_L}\right] \\ \frac{d\phi(t)}{dt} &= \mathrm{Im}[\xi](N(t) - N_{sol}) - \kappa\rho_{\gamma_L}\frac{\rho(t-\tau_{ext})}{\rho(t)}\sin[\omega_{sol}\tau_{ext} + \phi(t) - \phi(t-\tau_{ext}) + \phi_{\gamma_L}]\end{aligned}$$

The solitary laser solutions are w_{sol} and N_{sol}, while the stationary solutions w_s and N_s are evaluated in presence of feedback.

For the carriers equation

$$\frac{dN(\rho,\varphi,t)}{dt} = \frac{\eta_i I(\rho,\varphi,t)}{eV} - \frac{N(\rho,\varphi,t)}{\tau_e} - G_N\left[N(\rho,\varphi,t) - N_0\right]|E(\rho,\varphi,t)|^2$$

The starting point is the non projected equation and substituting $N(\rho, \varphi, t) = N(t)$ e $I(\rho, \varphi) = I$,

$$\frac{dN(t)}{dt} = \frac{\eta_i I}{eV} - \frac{N(t)}{\tau e} - \frac{v_g g_n}{N_0}[N(t) - N_0]\rho^2(t)$$

B.2 Stationary solution evaluation

In order to find the stationary solutions, the modulus of the electric field and the carriers should be fixed at a stationary value. For the phase, a detuning with respect to the angular frequency of the solitary laser should be introduced.

$$\rho(t) = \rho_s \quad N(t) = N_s \quad \phi(t) = (\omega_s - \omega_{sol})\, t$$

$$\begin{cases} \frac{d\rho(t)}{dt} = \frac{v_g g_n \Gamma}{2N_0}(N - N_{sol})\rho(t) + \frac{\kappa}{\tau_c}\rho(t - \tau_{ext})\cos[\omega_{sol}\tau_{ext} + \phi(t) - \phi(t - \tau_{ext})]. \\ \frac{d\Phi(t)}{dt} = \frac{\alpha v_g g_n \Gamma}{2N_0}(N - N_{sol}) - \frac{\kappa}{\tau_c}\frac{\rho(t-\tau_{ext})}{\rho(t)}\sin[\omega_{sol}\tau_{ext} + \phi(t) - \phi(t - \tau_{ext})] \\ \frac{dN(t)}{dt} = \frac{\eta_i I}{eV} - \frac{N(t)}{\tau_e} - \frac{v_g g_n}{N_0}\left[N(t) - N_0\right]\rho^2(t) \end{cases}$$

Substituting

$$0 = \frac{v_g g_n \Gamma}{2N_0}\left(N_s - N_{sol}\right)\rho_s + \frac{\kappa}{\tau_c}\rho_s \cos\underbrace{\left[\omega_{sol}\tau_{ext} + \phi(t) - \phi(t - \tau_{ext})\right]}$$

$$\omega_{sol}\tau_{ext} + (\omega_s - \omega_{sol})t - (\omega_s - \omega_{sol})(t - \tau_{ext}) =$$
$$= \omega_{sol}\tau_{ext} + \omega_s\tau_{ext} - \omega_{sol}\tau_{ext} = \omega_s\tau_{ext}$$

Substituting

$$\begin{cases} 0 = \frac{v_g g_n \Gamma}{2N_0}\left(N_s - N_{sol}\right)\rho_s + \frac{\kappa}{\tau_c}\rho_s\cos[\omega_s\tau_{ext}] \\ w_s - w_{sol} = \frac{\Gamma\alpha v_g g_N}{2N_0}\left(N_s - N_{sol}\right) - \frac{\kappa}{\tau_c}\frac{\rho_s}{\rho_s}\sin[\omega_s\tau_{ext}] \\ 0 = \frac{\eta_i I}{eV} - \frac{N_s}{\tau_e} - \frac{v_g g_N}{N_0}\left[N_s - N_0\right]\rho_s^2 \end{cases}$$

From the carriers equation is it possible to obtain ρ_s^2.

$$\frac{\eta_i I}{eV} - \frac{N_s}{\tau_e} = \frac{v_g g_N}{N_0}\left[N_s - N_0\right]\rho_s^2$$
$$\rho_s^2 = \left[\frac{\eta_i I}{eV} - \frac{N_s}{\tau_e}\right]\frac{N_0}{v_g g_N\left[N_s - N_0\right]}$$

From the equation of the modulus it is possible to obtain N_s.

$$\frac{\Gamma v_g g_N}{2N_0}\left(N_s - N_{sol}\right)\rho_s = -\frac{\kappa}{\tau_c}\rho_s\cos[\omega_s\tau_{ext}]$$
$$N_S = N_{sol} - \frac{2N_0}{\Gamma v_g g_N}\frac{\kappa}{\tau_c}\cos[\omega_s\tau_{ext}]$$

Substituting the N_s value inside the $\omega_s - \omega_{sol}$ equation

$$\omega_{sol} = \omega_s + \frac{\kappa}{\tau_c}[\alpha\cos(\omega_s\tau_{ext}) - \sin(\omega_s\tau_{ext})]$$

using

$$\begin{aligned}\sin(\omega_s\tau_{ext} + \arctan\alpha) =& \sin((\omega_s\tau_{ext})\cos(\arctan\alpha) + \cos((\omega_s\tau_{ext})\sin(\arctan\alpha))\\ =& \frac{\sin(\omega_s\tau_{ext})}{\sqrt{1+\alpha^2}} + \cos(\omega_s\tau_{ext})\frac{\alpha}{\sqrt{1+\alpha^2}}\end{aligned}$$

The resutl is

$$\omega_{sol} = \omega_s + \frac{\kappa}{\tau_c}\sqrt{1+\alpha^2}[\sin(\omega_s\tau_{ext} + \arctan\alpha)]$$

The equation obtained links the solitary laser frequency with the stationary solution.

B.3 Stability Analysis

Considering perturbations $\delta\rho(t), \delta\phi(t)$ e $\delta N(t)$ with respect to the stationary state. The starting point is the following system

$$\begin{cases}\frac{d\rho(t)}{dt} = \mathbb{R}[\xi](N - N_{sol})\rho(t) + \frac{\kappa}{\tau_c}\rho(t-\tau_{ext})\cos[\omega_{sol}\tau_{ext} + \phi(t) - \phi(t-\tau_{ext})]\\ \\ \frac{d\phi(t)}{dt} = \mathrm{Im}[\xi](N - N_{sol}) - \frac{\kappa}{\tau_c}\frac{\rho(t-\tau_{ext})}{\rho(t)}\sin[\omega_{sol}\tau_{ext} + \phi(t) - \phi(t-\tau_{ext})]\\ \\ \frac{dN(t)}{dt} = \frac{\eta_i I}{ev} - \frac{N(t)}{\tau_e} - \frac{v_g g_N}{N_0}\left[N(t) - N_0\right]\rho^2(t)\end{cases}$$

and substituting

$$\begin{cases} \rho(t) = \rho_s + \delta\rho(t) \\ \\ \phi(t) = \phi s + \delta\phi(t) = (\omega_s - \omega_{sol})t + \delta\phi(t) \\ \\ N(t) = N_s + \delta N(t) \end{cases}$$

$$\begin{aligned} \frac{d}{dt}[\rho s+\delta\rho(t)] &= \mathrm{Re}(N_s + \delta N(t) - N_{sol})[\rho_s + \delta\rho(t)] + \frac{\kappa}{\tau_c}[\rho_s + \delta\rho(t-\tau_{ext})]\cdot \\ &\cdot \cos[\omega_{sol}\tau_{ext} + (\omega_s - \omega_{sol})\,t + \delta\phi(t) - (\omega_s - \omega_{sol})\,(t-\tau_{ext}) - \delta\phi(t-\tau_{ext})] \\ &= \cos[\omega_s\tau_{ext} + \delta\phi(t) - \delta\phi(t-\tau_{ext})] = \\ &\simeq \cos(\omega_s\tau_{ext}) - [\delta\phi(t) - \delta\phi(t-\tau_{ext})]\sin(\omega_s\tau_{ext}) \end{aligned}$$

In order to obtain this equality, it is necessary to use the formula

$$\cos(A+B) = \cos A\cos B - \sin A\sin B \quad \text{con} \begin{cases} A = \omega_s\tau_{ext} \\ B = \delta\phi(t) - \delta\phi(t-\tau_{ext}) \end{cases}$$

Using the small angle approximation

$$\begin{cases} \cos\theta = 1 - \frac{\theta^2}{2} \simeq 1, \quad \text{(first-order approximation)} \\ \sin\theta = \theta \end{cases}$$

$$\begin{cases} \cos[\delta\phi(t) - \delta\phi(t-\tau_{ext})] = 1 \\ \sin[\delta\phi(t) - \delta\phi(t-\tau_{ext})] = \delta\phi(t) - \delta\phi(t-\tau_{ext}) \end{cases}$$

$$\begin{aligned} \delta\dot{\rho}(t) = &\,\mathrm{Re}\,\xi(N_s + \delta N(t) - N_{sol})[\rho_s + \delta\rho(t)] + \frac{\kappa}{\tau_c}[\rho_s + \delta\rho(t-\tau_{ext})]\cdot \\ &\cdot \{cos\,(\omega_s\tau_{ext} - [\delta\phi(t) - \delta\phi(t-\tau_{ext})]\sin(\omega_s\tau_{ext})\} \end{aligned}$$

$$\begin{aligned} \delta\dot{\rho}(t) = &\,\mathrm{Re}\,\xi[(N_s - N_{sol})\delta\rho(t) + \rho_s\delta N(t)] + \frac{\kappa}{\tau_c}[\delta\rho(t-\tau_{ext})\cos(\omega_s\tau_{ext}) + \\ &- \rho_s[\delta\phi(t) - \delta\phi(t-\tau_{ext})]\sin(\omega_s\tau_{ext})] \end{aligned}$$

Writing $I(t) = \rho^2(t)$

$$\begin{aligned} \delta I(t) &= (\rho s + \delta\rho(t))^2 = \rho_s^2 + (\delta\rho(t))^2 + 2\rho_s\delta\rho(t) \\ \delta\rho(t) &= \frac{\delta I(t)}{2\rho_s} \text{ and } \delta I(t) = 2\rho_s\delta\rho(t) \end{aligned}$$

Deriving $\delta I(t)$

$$\delta\dot{I}(t) = 2Is\left(\frac{\delta\dot{\rho}(t)}{\rho_s}\right) = 2Is\Bigg\{\operatorname{Re}\xi\left[(N_s - N_{sol})\frac{\delta\rho(t)}{\rho_s} + \delta N(t)\right] + \\ + \frac{\kappa}{\tau_c}\left[\frac{\delta\rho(t-\tau_{ext})}{\rho_s}\cos(\omega_s\tau_{ext}) - [\delta\phi(t) - \delta\phi(t-\tau_{ext})]\sin(\omega_s\tau_{ext})\right]\Bigg\}$$

Substituting $\delta\rho(t) = \frac{\delta I(t)}{2\rho_s}$

$$\delta\dot{I}(t) = \mathbb{R}\xi[(N_s - N_{sol})\delta I(t) + 2I_s\delta N(t)] + \frac{\kappa}{\tau_c}[\delta I(t-\tau_{ext})\cos(\omega_s\tau_{ext}) + \\ - 2I_s[\delta\phi(t) - \delta\phi(t-\tau_{ext})]\sin(\omega s\tau_{ext})]$$

Remembering the stationary solutions

$$N_s - N_{sol} = -\frac{1}{\operatorname{Re}\xi}\frac{\kappa}{\tau_c}\cos[\omega_s\tau_{ext}]$$

$$\delta\dot{I}(t) = \operatorname{Re}\xi\left[-\frac{1}{\operatorname{Re}\xi}\frac{\kappa}{\tau_c}\cos[\omega_s\tau_{ext}]\delta I(t) + 2I_s\delta N(t)\right] + \\ + \frac{\kappa}{\tau_c}\left[\delta I(t-\tau_{ext})\cos(\omega_s\tau_{ext} - 2I_s[\delta\Phi(t) - \delta\Phi(t-\tau_{ext})]\sin(\omega_s\tau_{ext})\right]$$

$$\delta\dot{I}(t) = 2Is\operatorname{Re}\xi\delta N(t) - \frac{\kappa}{\tau_c}[\delta I(t) - \delta I(t-\tau_{ext})]\cos(\omega_s\tau_{ext}) + \\ - 2I_s\frac{\kappa}{\tau_c}[\delta\phi(t) - \delta\phi(t-\tau_{ext})]\sin(\omega_s\tau_{ext})$$

Substituting the perturbations in the phase equation

$$\frac{d}{dt}[\Phi_s + \delta\Phi(t)] = \operatorname{Im}\xi(N_s + \delta N(t) - N_{sol}) - \frac{\kappa}{\tau_c}\frac{\rho_s + \delta\rho(t-\tau_{ext})}{\rho_s + \delta\rho(t)}\cdot \\ \cdot[(\delta\phi(t) - \delta\phi(t-\tau_{ext}))\cos(\omega_s\tau_{ext}) + \sin(\omega_s\tau_{ext})]$$

$$\delta\dot{\phi}(t) = \operatorname{Im}\xi\,(N_s + \delta N(t) - N_{sol}) - \frac{\kappa}{\tau_c}\left[1 + \frac{\delta\rho\,(t-\tau_{ext}) - \delta\rho(t)}{\rho_s}\right]\cdot \\ \cdot[(\delta\phi(t) - \delta\phi(t-\tau_{ext}))\cos\,(\omega_s\tau_{ext}) + \sin\,(\omega_s\tau_{ext})]$$

Substituting the stationary solution and the current

$$\delta\dot{\phi}(t) = \operatorname{Im}\xi\left[-\frac{1}{\operatorname{Re}\xi}\frac{\kappa}{\tau_c}\cos[\omega_s\tau_{ext}] + \delta N(t)\right] - \frac{\kappa}{\tau_c}\left[1 + \frac{\delta I(t-\tau_{ext}) - \delta I(t)}{2\rho_s\cdot\rho_s}\right] + \\ + [(\delta\phi(t) - \delta\phi(t-\tau_{ext}))\cos\,(\omega_s\tau_{ext})\ + \sin\,(\omega_s\tau_{ext})]$$

Remembering that $\xi = \frac{\Gamma v_g g_n}{2N_0}(1+i\alpha)$ $\left.\begin{array}{l} \rightarrow \mathrm{Re}\,\xi = \frac{\mathrm{v_g}\, g_n \Gamma}{2N_0} \\ \rightarrow \mathrm{Im}\,\xi = \frac{\mathrm{v_g}\, g_n \alpha \Gamma}{2N_0} \end{array}\right\}$ $\frac{\mathrm{Im}\,\xi}{\mathrm{Re}\,\xi} = \alpha$

$$\delta\dot{\phi}(t) = \mathrm{Im}\,\xi\delta N(t) - \frac{\kappa}{\tau_c}[(\delta\phi(t) - \delta\phi(t-\tau_{ext}))\cos(\omega_s\tau_{ext})] + \\ - \frac{\kappa}{\tau_c}\frac{\delta I(t-\tau_{ext}) - \delta I(t)}{2I_s}\sin(\omega_s\tau_{ext})$$

Substituting the perturbations in the carriers equation

$$\frac{d}{dt}[N_s + \delta N(t)] = \frac{\eta_i I}{eV} - \frac{N_s + \delta N(t)}{\tau_e} - \frac{v_g g_n}{N_0}[N_s + \delta N(t) - N_0](I_s + \delta I(t))$$
$$\delta\dot{N}(t) = -\Gamma_N \delta N(t) - \frac{v_g g_N}{N_0}(N_s - N_0)\delta I(t)$$

With $\Gamma_N = \frac{1}{\tau_e} - \frac{v_g g_n I_s}{N_s}$.

The obtained system is the following one

$$\begin{cases} \delta\dot{I}(t) = 2I_s\,\mathrm{Re}\,\xi\delta N(t) - \dfrac{\kappa}{\tau_c}\Big[\delta I(t) - \delta I(t-\tau_{ext})\Big]\cos(\omega_s\tau_{ext}) \\ \qquad\qquad - 2I_s\dfrac{\kappa}{\tau_c}\Big[\delta\Phi(t) - \delta\Phi(t-\tau_{ext})\Big]\sin(\omega_s\tau_{ext}), \\ \\ \delta\dot{\phi}(t) = \mathrm{Im}\,\xi\delta N(t) - \dfrac{\kappa}{\tau_c}\Big[\delta\Phi(t) - \delta\Phi(t-\tau_{ext})\Big]\cos(\omega_s\tau_{ext}) \\ \qquad\qquad - \dfrac{\kappa}{\tau_c}\dfrac{\delta I(t-\tau_{ext}) - \delta I(t)}{2I_s}\sin(\omega_s\tau_{ext}), \\ \\ \delta\dot{N}(t) = -\Gamma_N\delta N(t) - \dfrac{v_g g_N}{N_0}(N_s - N_0)\delta I(t). \end{cases}$$

Going to the frequency domain

$$\frac{d}{dt} \rightarrow i\tilde{\omega}$$
$$f(t-\tau_{ext}) \rightarrow F(\tilde{\omega})e^{-i\omega\tau_{ext}}$$

$$\imath\tilde{\omega}\delta I(\tilde{\omega}) = 2Is\,\mathrm{Re}\,\xi\delta N(\tilde{\omega}) - \frac{\kappa}{\tau_c}\left[\delta I(\tilde{\omega}) - \delta I(\tilde{\omega})e^{-i\tilde{\omega}\tau_{ext}}\right]\cos(\omega_s\tau_{ext}) + \\ - 2I_s\frac{\kappa}{\tau_c}\left[\delta\Phi(\tilde{\omega}) - \delta\Phi(\tilde{\omega})e^{-i\tilde{\omega}\tau_{ext}}\right]\sin(\omega_s\tau_{ext})$$

$$i\tilde{\omega}\delta I(\tilde{\omega}) = 2Is\,\mathrm{Re}\,\xi\delta N(\tilde{\omega}) - \frac{\kappa}{\tau_c}\left(1 - e^{-i\tilde{\omega}\tau_{ext}}\right)\delta I(\tilde{\omega})\cos(\omega_s\tau_{ext}) + \\ - 2Is\frac{\kappa}{\tau_c}\left(1 - e^{-i\tilde{\omega}\tau_{ext}}\right)\delta\phi(\tilde{\omega})\sin(\omega_s\tau_{ext})$$

$$\imath\tilde{\omega}\delta\phi(\tilde{\omega}) = \mathrm{Im}\,\xi\delta N(\tilde{\omega}) - \frac{\kappa}{\tau_c}\left(1 - e^{-i\tilde{\omega}\tau_{ext}}\right)\delta\phi(\tilde{\omega})\cos\left(\omega_s\tau_{ext}\right) + \\ - \frac{\kappa}{\tau_c}\frac{\left(1 - e^{-i\tilde{\omega}\tau_{ext}}\right)\delta I(\tilde{\omega})\sin\left(\omega_s\tau_{ext}\right)}{2I_s}$$

$$i\tilde{\omega}\delta N(\tilde{\omega}) = -\Gamma_N\delta N(\tilde{\omega}) - \frac{\mathrm{v_g}\, g_N}{N_0}(N_s - N_0)\delta I(\tilde{\omega})$$

The Jacobian matrix will be

$$M(\delta I(\tilde{\omega}), \delta\Phi(\tilde{\omega}), \delta N(\tilde{\omega})) = 0$$

$$\mathbf{M} = \begin{bmatrix} -\frac{\kappa}{\tau_c}(1 - e^{-i\tilde{\omega}\tau_{ext}})\cos(\omega_s\tau_{ext}) & -2I_s\frac{\kappa}{\tau_c}(1 - e^{-i\tilde{\omega}\tau_{ext}})\sin(\omega_s\tau_{ext}) & 2I_s\Re(\xi) \\ \frac{\kappa}{\tau_c}\frac{(1-e^{-i\tilde{\omega}\tau_{ext}})}{2I_s}\sin(\omega_s\tau_{ext}) & -\frac{\kappa}{\tau_c}(1 - e^{-i\tilde{\omega}\tau_{ext}})\cos(\omega_s\tau_{ext}) & \Im(\xi) \\ -\frac{v_g g_n}{N_0}(N_s - N_0) & 0 & -\Gamma_N \end{bmatrix}$$

Bibliography

[1] Rainer Michalzin. *Fundamentals, technology and applications of vertical-cavity surface-emitting lasers*. Springer, 2013 (cit. on p. 2).

[2] Cristina Rimoldi, Lorenzo L. Columbo, Alberto Tibaldi Member IEEE, Pierluigi Debernardi, Sebastian Romero García, Christian Raabe, and Mariangela Gioannini. «Impact of Coherent Mode Coupling on Noise Performance in Elliptical Aperture VCSELs for Datacom». In: *IEEE JOURNAL OF SELECTED TOPICS IN QUANTUM ELECTRONICS, VOL. 31, NO. 2* (MARCH/APRIL 2025) (cit. on pp. 2, 5, 6, 8, 14, 15, 21, 63).

[3] D. Gazula, N. Chitica, M. Chacinski, G. Landry, and J. Tatum. «VCSEL with elliptical aperture having reduced RIN». In: *U.S. Patent 20190341743A1,* (Mar. 21, 2019) (cit. on p. 2).

[4] B. Wang, W. Sorin, S. Mathai M. Tan, and S. Cheung. «Intensity noise mitigation for vertical-cavity surface emitting lasers». In: *U. S. Patent 10985531B2* (Apr. 20, 2019) (cit. on p. 2).

[5] P. Debernardi, G. Bava, C. Degen, I. Fischer, and W. Elsasser. «Influence of anisotropies on transverse modes in oxide-confined VCSELs». In: *IEEE J. Quantum Electron., vol. 38, no. 1, pp. 73–84* (Jan. 2002) (cit. on p. 2).

[6] Larry A. Coldren, Scott W. Corzine, and Milan L. Masanovic. *Diode Lasers and Photonic Integrated Circuits*. A Jonhn Wille and sons INC. Pubblication, 2012 (cit. on pp. 13, 14).

[7] R. Lang and K. Kobayashi. «External optical feedback effects on semiconductor injection laser properties». In: *IEEE J. Quantum Electron. 16* (1980) (cit. on pp. 26, 58).

[8] Deborah M. Kane and K.Alan Shore. *Unlocking dynamical diversity, optical feedback effects on semiconductor lasers*. John Wiley and sons, Ltd, 2005 (cit. on pp. 27–29, 50, 66).

[9] Joanne Y. Law, Govind P. Agrawal, and Fellow. «Effects of Optical Feedback on Static and Dynamic Characteristics of Vertical-Cavity Surface-Emitting Lasers». In: *IEEE J. Quantum Electron., vol. 3, no. 2* (April 1997) (cit. on pp. 50, 53, 57).